SECTION III

Mechanistic Details of the Operation of DSCs

CHAPTER 11

DYNAMICS OF INTERFACIAL AND SURFACE ELECTRON TRANSFER PROCESSES

Jacques-E. Moser

Photochemical Dynamics Group

Institute of Chemical Sciences and Engineering

Ecole Polytechnique Fédérale de Lausanne

CH-1015 Lausanne, Switzerland

About the author

Jacques-E. Moser obtained in 1982 a diploma degree (MSc) in chemical engineering and in 1986 a doctorate in sciences (PhD) from the Ecole Polytechnique Fédérale de Lausanne (EPFL) with a thesis carried out under the supervision of Prof. Michael Grätzel. In 1986 he joined the Eastman Kodak Corporate Research Laboratories in Rochester (NY, USA) and was then associated with the newly created NSF Center for Photoinduced Charge Transfer at the University of Rochester (Prof. Samir Farid). He was appointed lecturer of physical chemistry at EPFL in 1992 and was awarded the habilitation in 1998. Jacques-E. Moser is titular professor since 2005 and is currently heading the School of Chemistry and Chemical Engineering of EPFL.

CHAPTER 11

DYNAMICS OF INTERFACIAL AND SURFACE ELECTRON TRANSFER PROCESSES

11.1 INTRODUCTION

In nanodispersed semiconductors, no significant space charge layer can establish within particles whose dimensions are inferior to the Debye length. Rather than relying on an electric field, sustained light-induced charge separation in bulk heterojunction photovoltaic devices is based on the kinetic competition between energy- and electron transfer and charge transport processes.

In dye-sensitized solar cells (DSCs), ultrafast electron injection from a molecular excited state into the conduction band of a wide-bandgap semiconductor is key to the initial interfacial light-induced charge separation, as it has to compete efficiently with fast radiative and nonradiative deactivation pathways and quenching reactions. Subsequently, dye cations produced by charge injection have to be intercepted prior to their recombination with conduction band electrons. This charge transfer between the oxidized sensitizer at the surface and the hole transporting medium defines in a great extend the photon-to-current conversion efficiency of the solar cell. Percolation of electrons between semiconductor nanoparticles, as well as hole transport within the pores network to the cathode, have finally to take place fast enough, as to prevent indirect electron-hole recombination.

Figure 11.1 shows in a schematic way the relevant photophysical processes and electron transfer steps involving a dye-sensitizer molecule adsorbed on the surface of a wide-bandgap semiconductor (S | SC) in the presence of a redox mediator (D).

a)	$S \mid SC + h\nu \rightarrow S^* \mid SC$	Photoexcitation	(11.1)
b)	$S^* \mid SC \rightarrow e^-_{cb}\,(SC) + S^+ \mid SC$	Electron injection	(11.2)
c)	$S^* \mid SC \rightarrow S \mid SC + h\nu' + \nabla$	Excited state deactivation	(11.3)
d)	$e^-_{cb}\,(SC) + S^+ \mid SC \rightarrow S \mid SC$	Back electron transfer	(11.4)
e)	$S^+ \mid SC + D \rightarrow S \mid SC + D^+$	Dye regeneration	(11.5)
f)	$D^+ + e^-_{cb}\,(SC) \rightarrow D$	Indirect charge recombination	(11.6)

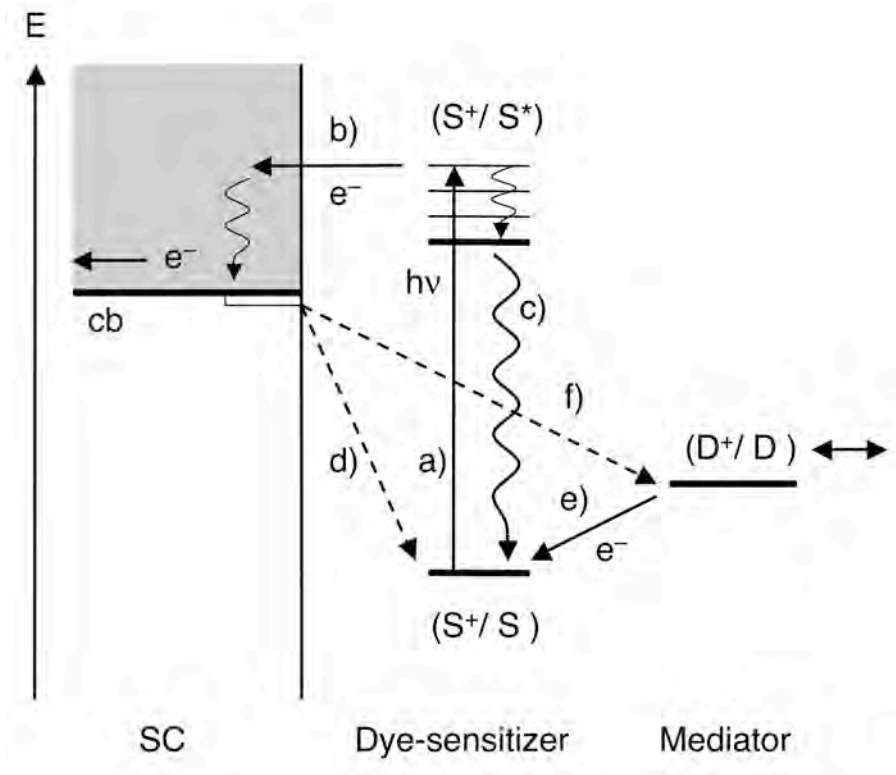

Figure 11.1 Energetic scheme of electron transfer processes taking place after charge injection from a molecular electronic excited state S* to the conduction band (cb) of a semiconductor (SC). Dashed arrows represent electron-hole recombination reactions that counter sustained charge separation.

The yield η_a of a first-order kinetic reaction occurring in parallel with a second reactive pathway is given by the simple relationship:

$$\eta_a = \frac{k_a}{k_a + k_b} \tag{11.7}$$

where k_a and k_b are the respective first-order rate constants of both parallel processes. Hence, a reaction *a* will take place almost quantitatively ($\eta_a \geq 0.99$) provided its rate constant is at least two orders of magnitude larger than that of a kinetically competitive process *b* ($k_a \geq 99 \times k_b$).

Dye-sensitizers, which do not undergo significant intersystem crossing, are characterized by excited state lifetimes typically in the range of $\tau = 10$ - 100 ps. In such conditions, efficient charge injection should clearly take place within a sub-picosecond time frame. Triplet MLCT excited states of Ru(II) polypyridyl complex sensitizers are usually much longer lived, with $\tau = 10$ - 100 ns. In the presence of concentrated electrolytes, however, fast quenching reactions often occur in the ps time scale. Femtosecond electron injection is therefore generally required to ensure efficient initial light-induced interfacial charge separation.

The rate of the electron recapture, which takes place between the solid and the oxidized dye species S^+ (Eq. 11.4), is usually observed to be slower by several orders of magnitude compared to charge injection rates of efficient sensitizers. In the N-719 | TiO_2 system, this back electron transfer process typically occurs in the hundreds of μs to ms time scale. This slow charge recombination process can be intercepted by reaction of a reducing mediator with the oxidized dye (Eq. 11.5). DSCs based on the sensitization of mesoporous titanium dioxide by Ru(II) complex dyes in conjunction with the I_3^- / I^- redox couple as a mediator have proved very efficient at exploiting this principle. However, oxidation of I^- to I_2 or I_3^- is a two-electron redox process and is intrinsically slow. Relatively high concentrations of iodide are thus necessary.

Figure 11.2 shows, as an example, the temporal evolution of the oxidized state S^+ of the complex dye sensitizer *cis*-$[Ru^{II}(dcbpyH)_2(NCS)_2]^{2-}$ (N-719). S^+ species is initially formed during photoinduced electron injection and later decays due to reduction by a mediator or charge recombination. In this particular case, kinetic competition between processes d) and e) (Eqs. 11.4, 11.5) is minimal and results in the formation of a long-lived charge separated state (e_{cb}^-… D^+) with nearly unity quantum yield.

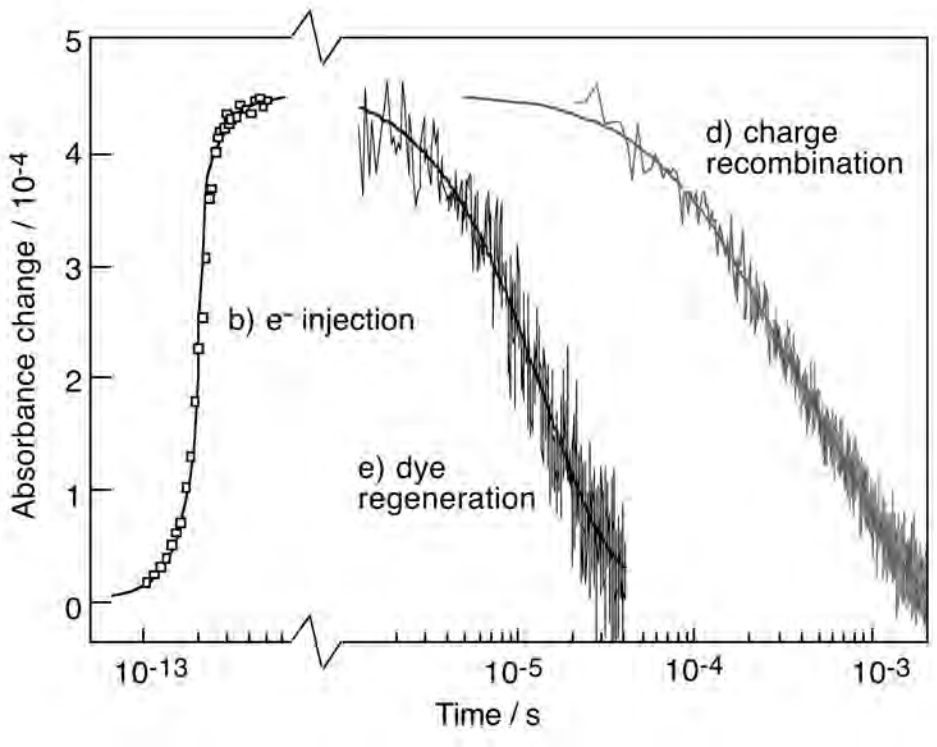

Figure 11.2 Transient absorbance signals recorded upon pulsed laser excitation of N-719 | TiO_2. Optical signals reflect the appearance and decay of the oxidized state S^+ of the dye. Data points at the shorter time scale corresponds to the electron injection process and concomitant formation of the S^+ species (Eq. 11.2). The decay curve at shorter time scale was obtained in the presence of a liquid electrolyte containing 0.8 M I^- and is indicative of the dye regeneration reaction (Eq. 11.5). The decay curve at longer time scale is due to the back electron transfer (Eq. 11.4) and was recorded in a pure redox-inactive solvent. Ultrafast transients were measured at a probe wavelength of 860 nm, following pumping at 535 nm. Ns-μs data were obtained at $\lambda = 680$ nm upon 600 nm pulsed laser excitation [1].

A thorough understanding of the functioning of successful DSCs, and perhaps even more importantly of the details of the mechanisms resulting in a bad performance, can be gained by the study of the dynamics of individual surface electron transfer reactions and charge transport processes. The knowledge acquired in performing time-resolved analysis of such phenomena is directly relevant for the improvement of existing systems, and the design of new strategies to achieve higher energy conversion efficiencies and a better stability of devices. Parameters influencing the kinetics of the electron injection, charge recombination and dye-cation interception reactions and their interplay have recently been reviewed [2].

11.2 ENERGETICS OF CHARGE TRANSFER REACTIONS

Knowledge of the relative positions of the energy level of reactants is essential for the understanding of the electron transfer dynamics. The energy gap between the interacting levels represents the nuclear reorganization barrier to attaining a condition of resonance. This thermodynamic aspect, along with nuclear relaxation dynamics and electron coupling, define the kinetics of charge transfer reaction.

Surface redox processes can occur with either adsorbed or dissolved reactants. As electron transfer with solution species cannot be faster than allowed by the diffusion, this limitation is not encountered in the adsorbed state. For excited molecules in solution, the deactivation processes are generally much faster than the average diffusion time to the surface. Hence, efficient charge injection can only take place in the adsorbed state. Static quenching of the sensitizer and re-reduction of oxidized species also depend critically on the association of the mediator ions with the dyed surface. Adsorption processes at the interface are therefore very important in defining both the thermodynamics and the kinetics of key charge transfer reactions.

11.2.1 Mesoscopic metal oxide semiconductors

Adsorption of ions and molecules on the surface

Electrophoretic measurements applied to dispersions in organic solvents of titanium dioxide scratched from sintered mesoscopic films show that nanoparticles are consistently negatively charged. Zeta-potential of naked TiO_2 surface in pure ethanol is measured as being typically $\zeta \cong -45$ mV, with little variation upon the preparation method. The oxide having been calcinated for several minutes at 450°C, its surface is essentially dehydroxylated. The negative charge is then probably due to Cl^- impurities originating from the $TiCl_4$ precursor, or to Cl^- and NO_3^- anions incorporated in the oxide when hydrochloric or nitric acids are used for the peptization of particles during the preparation of the TiO_2 paste. In such conditions, electrostatic interactions should oppose the approach of anions to the surface. Efficient adsorption of anionic carboxylated dye species, such as $[Ru^{II}(NCS)_2(dcbpyH)_2]^{2-}$ (N-719), is however observed on the surface of TiO_2. Chemisorption in this case clearly overcomes the electrostatic repulsion and renders the derivatized oxide surface even more negatively charged, with zeta-potentials establishing finally around $\zeta \cong -54$ mV at saturation.

Surface of oxides are characterized by the presence at the crystal boundary of metal centers which are not coordinatively saturated by the oxygen atoms of the lattice. Their surface concentration on TiO_2 (anatase) nanoparticles, for instance, was measured to be $\Gamma = 7\ \mu mol \cdot m^{-2}$ [3]. These surface cations can coordinate to oxygen-containing molecules like water or alcohols, and to anions. Ti^{IV}, Zr^{IV}, Nb^{V} or Al^{III} metal centers, and to a lesser extend Zn^{II}, are indeed strong Lewis acids and show a particular affinity for hard bases. The adsorption strength of the anions therefore depends on their Lewis basicity, in the typical order $F^- > \text{oxoanions} > Cl^- > Br^- > I^- > I_3^- > (CF_3SO_2)_2N^-$. Among oxoanions, large basicity differences exist, which translate into various

affinities for the metal oxide surfaces. Hard oxoanions, *i.e.* with high charge density and low polarizability, bind stronger than soft oxoanions. The following affinity series can be observed: $OH^- > PO_4^{3-} > R\text{–}PO_3^{2-} > R\text{–}COO^- > R\text{–}SO_3^- > ClO_4^- > CF_3SO_3^-$. Even though the binding constants of these anions were not all measured, qualitative observation of substitution processes on the metal oxide surface allow for the above classification. In addition, chelation processes can be invoked to account for the particular surface affinity of several bidentate ligands, like catecholate, salicyate or acetylacetonate.

Except in the case where the absorbed species are prone to the formation of aggregates, adsorption isotherms on nanocrystalline metal oxide show clean Langmuir behavior and can be fitted with the corresponding equation (Eq. 11.8), where C is the concentration of the species in solution, Γ^0 its surface concentration in a saturated monolayer and K [M^{-1}] is the adsorption equilibrium constant.

$$\Gamma = \frac{\Gamma^0 C}{C + \frac{1}{K}} \tag{11.8}$$

In dry ethanol, the adsorption equilibrium constant K for the dye-sensitizer $Ru(NCS)_2(dcbpyH)_2(NBu_4)_2$ (N-719) is in the order of $K = 5 \cdot 10^4$ M^{-1}, while the value of Γ^0 ranges between 1-7 $\mu mol \cdot m^{-2}$, depending on the degree of protonation of the dye and/or of the surface. The adsorption constants and surface concentration at full coverage show a clear solvent dependence [4], which can be rationalized in terms of competition between adsorption and solvation of the solute on the one hand, as well as of competition between the adsorption of the solvent and that of the solute, on the other hand. Carboxylated xanthene dyes such as dichlorofluorescein or eosin offer in this respect an exemplary illustration of the effect of the solvent on the mechanism of adsorption. Figure 11.3 displays the 3D-structure of anionic eosin-Y adsorbed on the surface of titanium dioxide. When TiO_2 is dehydroxylated, such as after calcination at

high temperature, adsorption takes place through the coordination of surface Ti(IV) acidic sites by the carboxylate fonction carried by eosin anion. In aqueous acidic medium the titanium dioxide surface is positively charged, due to the protonation of bridge oxygen atoms and amphoteric hydroxyl end groups. In this case, adsorption of eosin anions takes place essentially through electrostatic interactions and possibly H-bonding. Water molecules could also form an additional solvation layer between the charged surface and the adsorbate. In this case, the distance between the first accessible Ti(IV) surface ions and the conjugated π-system of the dye molecule is considerably increased as compared to the case of eosin adsorbed on the dehydroxylated surface. This change in the adsorption geometry results in a marked increase of the time constant for electron injection from photoexcited xanthene dye molecules into the conduction band of TiO_2 by at least one order of magnitude, from typically $\tau_{inj} < 30$ fs in case A [5] to $\tau_{inj} \geq 300$ fs in case B [6].

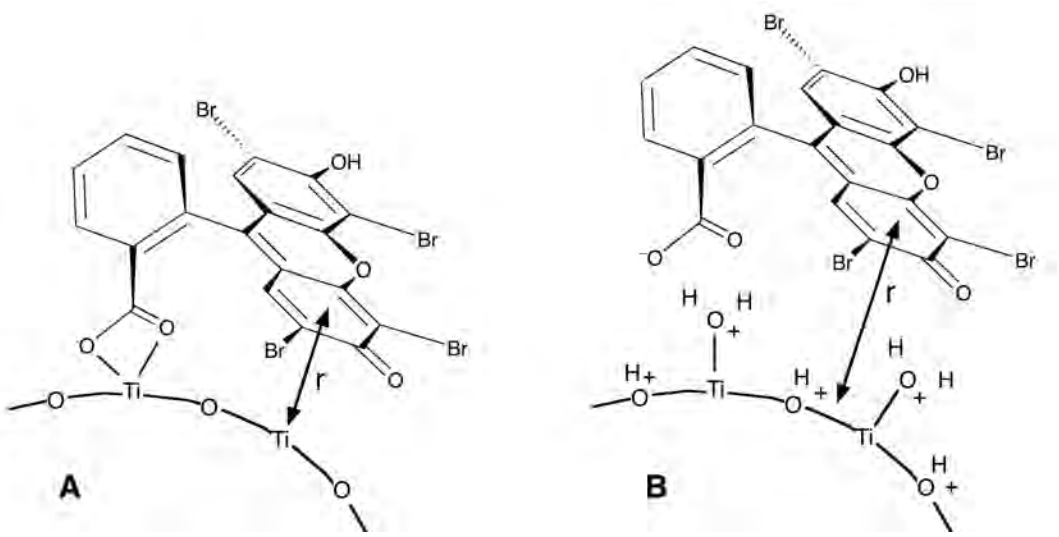

Figure 11.3 Structure of the anionic form of eosin-Y dye adsorbed on the surface of dehydroxylated TiO_2 in a dry organic solvent (**A**), and on that of an hydroxylated oxide surface in acidic water (**B**). Tridimensional structure of the dye was obtained from a MOPAC semiempirical quantum mechanical calculation.

Energetics of the semiconductor-liquid interface

Three important thermodynamic parameters for the electrochemical behavior of a semiconductor-liquid electrolyte heterojunction are the conduction band edge potential ϕ_{cb}, the flat-band potential ϕ_{fb}, which is equal to the conduction band edge potential at the interface, and the Fermi energy level E_F. The potential corresponding to the Fermi level ($\phi_F = -E_F / \mathcal{F}$, where $\mathcal{F}$ is the Faraday constant) can be considered as the electrochemical potential of electrons in the semiconductor. The conduction band edge represents the potential at which the first metallic center (with the exception of intraband trap states) can be reduced.

Apart from the semiconductor material, the energy of the conduction band edge depends on the nature and composition of the electrolyte. Specific adsorption of ions can shift the flat-band potential significantly. For metal oxide semiconductors/ aqueous solution interfaces, protonation and deprotonation of amphoteric sites causes a – 60 mV cathodic shift in ϕ_{fb} for every increase of the solution *pH* by one unit [7,8]. Values for the flat-band potential were determined for TiO_2 [9-11] by measuring the absorbance of the conduction band electrons as a function of applied potential. A Nernstian behavior was observed with ϕ_{fb} [V/NHE] = $-0.14 - 0.06$ pH in aqueous medium. More recent findings suggest proton intercalation can also play an important role [12]. Adsorption of other potential determining species, like Li^+ [11,13] and Mg^{2+} also affect ϕ_{cb}, while other small cations (K^+, Na^+) and anions (I^-, dyes) [13], surfactant molecules and surface complexing agents, influence the zeta-potential of the semiconductor. On many oxide surfaces the density of charged sites present at the isoelectric point (PZZ) is rather low. As the solid is charged up by adsorption of potential-determining ions, the environment in which the ions find themselves is significantly changing. Consequently, the Nernst equation does not hold in general, and a prediction of the surface potential is a quite difficult and risky exercise.

Measurements in non-aqueous solutions have revealed that ϕ_{fb} is directly related to the Brønsted acidity of the solvent [11]. A distinction between protic and aprotic solvents is therefore more appropriate than between aqueous and nonaqueous media. In aprotic solvents like CH_3CN, ϕ_{fb} is very negative (as much as – 2 V/ SCE for TiO_2) [14], but can be raised up to 0 V by adsorption of hard cations like H^+, Li^+ or Mg^{2+}, able to compensate the charges trapped on the surface [11].

The flat-band potential is determined by ions adsorbed on the surface and by surface states. These states correspond to surface metal ions for which, because of incomplete coordination, the redox potential lies within the bandgap of the oxide. As soon as electrons from the conduction band or from the solution reduce the surface states, they get trapped and can only escape by transfer to an oxidizing species across the interface, by light excitation or by hopping on the surface. On single-crystal TiO_2 rutile, for instance, $Ti^{IV/III}$ surface states can be found 0.8 eV below the conduction band edge [15]. For nanocrystalline particles, a broad distribution of surface states potentials is expected, corresponding to the multiplicity of lattice planes at the surface, with a suggested preferential localization of the traps at grain boundaries [10].

Figure 11.4 schematizes the energetics of electron transfer for an *n*-doped semiconductor in contact with three different redox couples (A^+/A, B^+/B, and C^+/C) in solution. The situation is depicted as a function of a cyclic potential scan, for large particles (a–f), and for a nanocrystalline assembly (a'–c'), respectively. The scan is started at a positive potential with all solution species in the oxidized state (a). At that potential ($\phi_F > \phi_{fb}$), the conduction band is lowered by the electric field, while the potential at the interface determined by surface states is fixed. A positive band bending results, which acts as a barrier for the electron transfer, of a height equal to $\phi_{fb} - \phi_F$. Thus, although the Fermi potential lies below $\phi°$ (C^+/C), reduction of C^+ does not occur rapidly. Excursion of the electrode potential into the flat-band region (b) results in the reduction of both B^+ and C^+ within a small potential range. If the electrode potential is

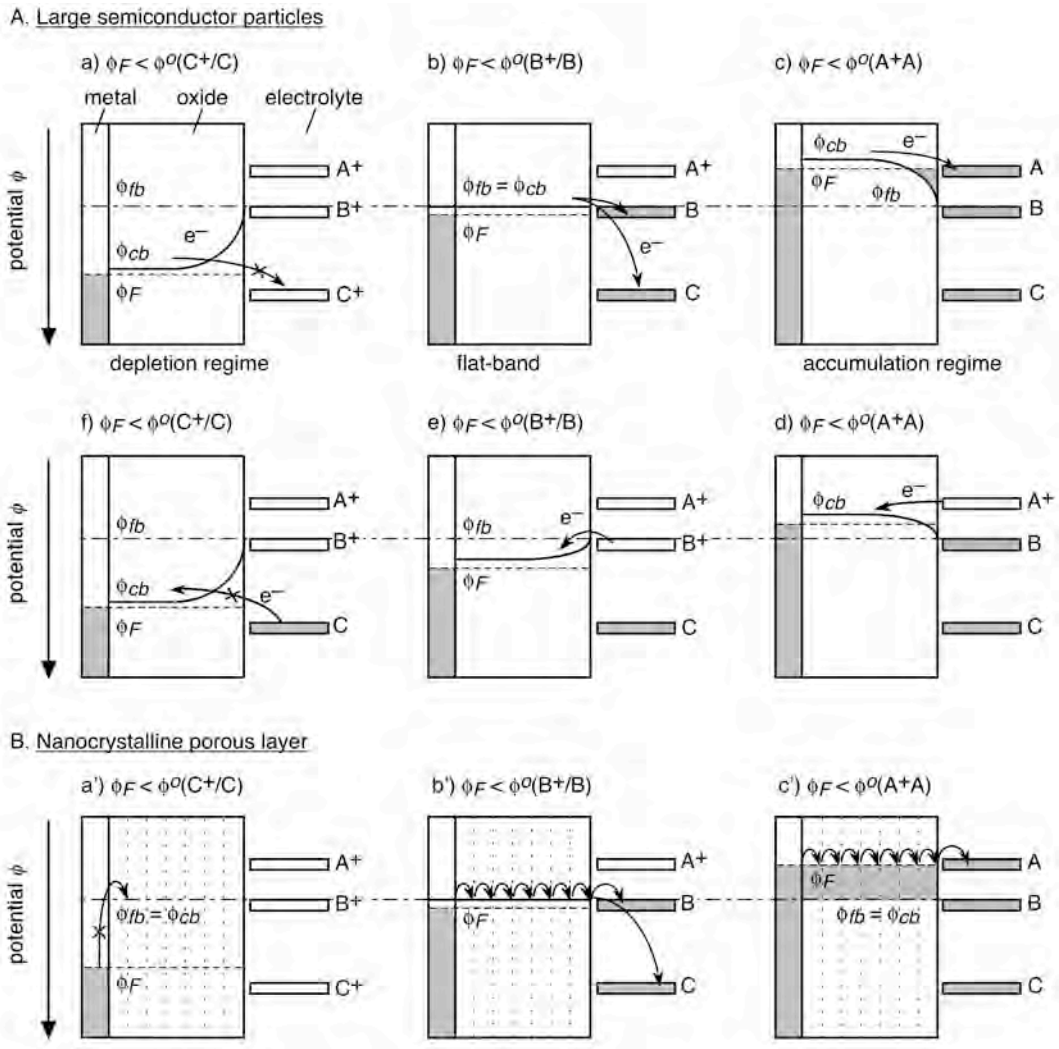

Figure 11.4 Schematic representation of the interfacial electron transfer processes between the conduction band of a semiconductor and electroactive species on the surface, during the cyclic sweeping of the electrode potential (a) → (b) → (c) → (d) → (e) → (f).

driven negative to ϕ_{fb}, the electric field causes an upwards band bending (accumulation layer) and the electrode exhibits metallic behavior for the species with $\phi^o < \phi_{fb}$, like the (A^+/A) couple, which is easily reduced (c) and again oxidized upon reversal of the potential scan direction (d). If the electrode potential is driven positive just below the flat-band situation, oxidation of B is observed (e). At more positive electrode potentials,

positive band bending develops (f). Oxidation of C is expected from thermodynamics as $\phi_F < \phi^o$ (C^+/C), but the activation barrier $\phi_{fb} - \phi^o$ (C^+/C) prevents fast charge injection into the semiconductor. As a result, the charge on the weak donor species C is kinetically trapped.

The above description is valid only for semiconductor particles larger than the width of the accumulation or depletion layer. Once the particle size decreases below that limit, band bending progressively vanishes, and the conduction band level eventually coincides with the flat band potential, reflecting the fact that the electric field created by the species present on the surface extends inside the whole particle. The total potential drop between the surface and the center of a spherical nanoparticle of radius *r* is obtained by solving the Poisson-Boltzmann equation and can be expressed by:

$$\Delta\phi = \frac{kT}{6e} \cdot \frac{r}{L_D} \tag{11.9}$$

where:

$$L_D = \sqrt{\frac{\varepsilon \cdot \varepsilon_0 \cdot kT}{2e^2 \cdot n_0}} \tag{11.10}$$

is the Debye length, which depends upon the static dielectric constant $\varepsilon \cdot \varepsilon_0$ of the material and the carrier density n_0 [16]. From Eq. 11.9 it is apparent that the electric field in semiconductor nanoparticles is usually small and/or that high dopant levels are required to produce a significant band bending inside the particle. A flat band situation indeed prevails when charge migration is negligible compared to thermal diffusion ($\Delta\phi < kT/e$). According to Eq. 11.9, this condition implies $r < \sqrt{6}\, L_D$. In the case of TiO_2 anatase particles, assuming a static dielectric constant $\varepsilon = 130$ and a carrier density $n_0 = 10^{17}$ cm^{-3}, then $L_D = 30$ nm and $r < 73$ nm. If the amount of majority carriers depleted from a semiconductor and the particle size are too small to develop a space

charge layer, the potential difference resulting from the charge transfer across the semiconductor / electrolyte interface must then drop in the Helmoltz layer. As a consequence, the position of the band edges of the particulate material are expected to shift cathodically upon electron injection and to move back during charge recombination [17].

This situation prevails in nanocrystalline films, where the typical particle size is of the order of 10-20 nm. As the conduction band is flat ($\phi_{cb} = \phi_{fb}$), it is more appropriate to use the conduction band potential ϕ_{cb} as a reference rather than ϕ_{fb}. When a positive potential ($\phi_F > \phi_{cb}$) is applied to the contact electrode, electrons deplete from the material turning it into an insulator. As soon as $\phi_F < \phi_{cb}$, electrons start to percolate inside the nanocrystalline film. The applied field drops in the accumulation layer formed near the particle surface and in the Helmholtz layer on the side of the electrolyte. Thus, the salient characteristics of a particulate film compared to the bulk semiconductor is the absence of an electric field across the material. Consequently, electrons do not migrate in particle assemblies, but diffuse in a random walk process.

Intraband trap states

Energy states lying below the conceptual bottom edge of the conduction band obviously complicate the energetic scheme described to this point for interfacial electron transfer reactions. Most of semiconducting metal oxide materials used in heterogeneous light-induced charge transfer reactions contain more or less abundant trapping sites in the bulk and at the surface. The presence of point defects like oxygen vacancies, and interstitial metal ions are indeed hardly avoidable, even in single crystal oxides. Coordinatively unsaturated surface metal ions represent efficient electron traps. Because of their large surface area to volume ratio, such surface states are quantitatively important in small nanocrystallites. For example, in a TiO_2 particle of 10 nm radius, as much as 6 % of all Ti(IV) ions are actually exposed at the surface. In mesoporous metal

oxide electrodes, where nanocrystalline particles are sintered together, grain boundaries are similar to dislocations and constitute two-dimensional arrays of oxygen vacancies. In zinc oxide, luminescence experiments showed that electron trap sites are mainly surface states [18-20], while photo-electrochemical studies on nanocrystalline Fe_2O_3 hematite demonstrated that, despite the large surface to volume ratio characterizing films constituted of particles in the 25-75 nm size range, capture of carriers by bulk and/or grain boundary traps is dominant [21].

Application of thermoluminescence, EPR [22-24] and impedance techniques [15]; to single crystal and colloidal TiO_2 led to the conclusion that at least eight different types of traps are active in this material, which energetic levels range from 0.2 to 0.9 eV below the conduction band edge. In addition, the existence of extended states near the mid-band gap region, at about 1.4 - 1.5 eV below the conduction band edge, has been suggested and discussed in terms of Ti–OH species [25].

Impedance and photocurrent spectroscopy studies using mesoporous anatase electrodes have reached similar conclusions [26]. Results obtained with transparent nanocrystalline films (Fig. 11.5) actually suggest that a continuum of trap levels is present near the conduction band edge that is characterized by a distribution of trap depths [9,27,28]. Such a band tail of localized states is commonly observed in disordered or amorphous materials, where it is generally more appropriate to talk about a mobility edge rather than a conduction band edge.

The importance of trapping sites on the dynamics of the charge recombination process in dye-sensitized nanocrystalline electrodes has been established by experiments carried out under externally applied electrical potential [29-31]. Biasing the Fermi level of TiO_2 positive to the flatband potential allows to control the occupancy of localized states lying below the conduction band edge of the semiconductor and to study the influence of traps on injection and recombination processes. The nature and

the amount of species adsorbed on the surface of the solid have also been shown to influence the population and energetics of surface states [3].

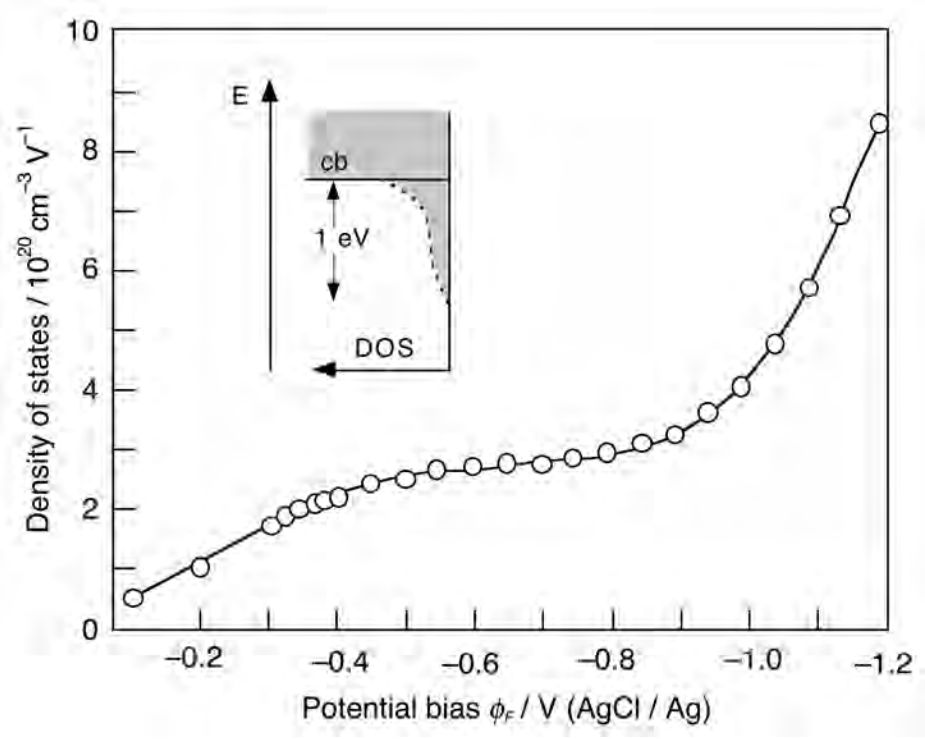

Figure 11.5 Density of electronic states near the conduction band edge of nanocrystalline TiO_2 anatase as a function of the applied potential. Data were derived from the measurement of the absorbance at $\lambda = 850$ nm of a transparent film electrode under potentiostatic control, with the assumption that all accumulated electrons are characterized by a decadic molar extinction coefficient $\varepsilon = 10^6$ mol$^{-1}\cdot$cm^2. The TiO_2 film was incorporated as a working electrode in a three electrodes spectro-electrochemical cell. 10^{-2} M tert-butylammonium triflate in anhydrous propylene carbonate was used as the electrolyte and the solution thoroughly degassed by repeated freeze-pump-thaw cycles [27].

Figure 11.6 illustrates how trap states present in a titanium dioxide nanocrystalline film can favor sustained light-induced charge separation in slowing down recombination following initial electron injection from a dye-sensitizer [29]. First order rate constants k_b characterizing the back electron transfer from the conduction

band to the oxidized state of a Ru(II) polypyridyl complex (Eq. 11.4) were obtained from time-resolved laser photolysis studies. When an anodic bias is applied to the TiO_2 electrode ($\phi_F >> \phi_{fb}$), trap states present in the bulk of the solid and at the surface are emptied.

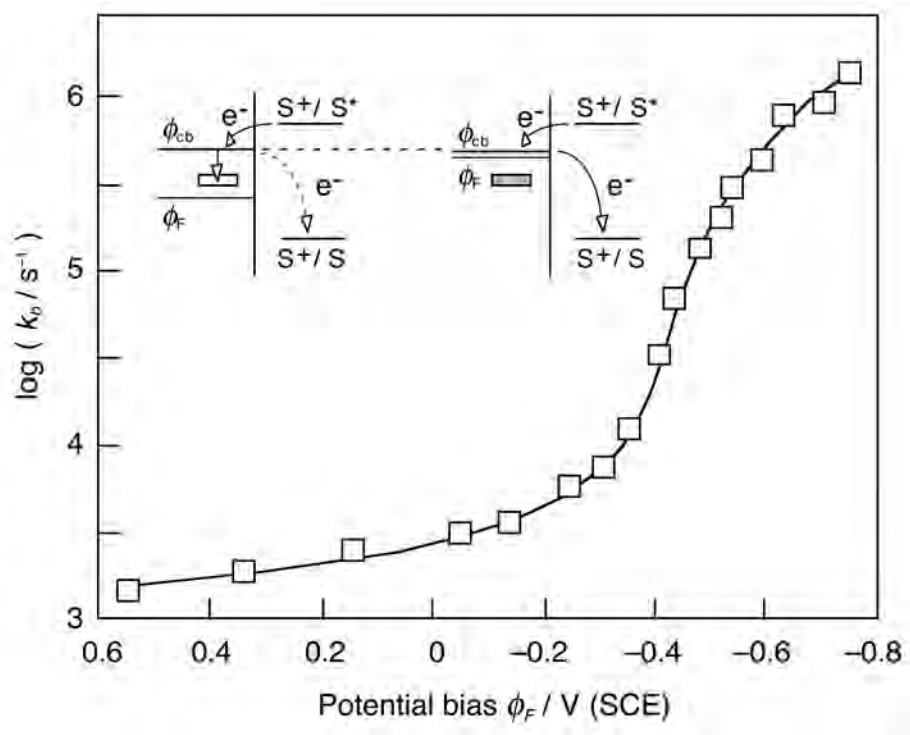

Figure 11.6 Effect of the electrochemical potential bias applied to a nanocrystalline TiO_2 photoanode sensitized by $Ru^{II}(dcbpy)_3^{2+}$ complex dye on the first order rate constant for the recombination of conduction band electrons with the oxidized sensitizer species $Ru^{III}(dcbpy)_3^{3+}$.

Electrons injected in the conduction band from photoexcited sensitizer molecules get thermalized to the bottom of the band and eventually fall into those empty traps. Transfer from these localized states to electron acceptors at the surface is hindered by the barrier represented by the energy requested to excite trapped carriers up to the conduction band level. As a result, recombination of injected electrons with oxidized

state of the dye is a rather slow process. Polarizing the TiO_2 film from + 0.6 V / SCE to – 0.8 V / SCE, where $\phi_F \cong \phi_{fb}$, progressively fills trap states lying below the conduction band. Photoinjected electrons cannot be trapped anymore and recombine much faster with dye cations at the surface. The rise of the value of the rate constant k_b by a factor of 1000 over the same voltage range is observed, the increase being steeper in the vicinity of the flatband potential. Further lowering of the bias potential eventually results in an accumulation situation, where $\phi_F < \phi_{fb}$, turning the TiO_2 film into a cathode.

Since surface electron traps arise mainly from incomplete coordination of metal ions present at the interface, coordination of these sites by adsorbates having a Lewis base character tends to raise the energy of the surface states. If the electron density of the ligand is strong enough, the electronic levels of the intraband states can eventually be raised into the conduction band, implying that their trapping action will vanish. Such an effect is likely to occur on the surface of dye-sensitized titanium dioxide. Dehydroxylated surface Ti(IV) indeed constitute electron traps, which energy level is situated about 200 meV lower than the conduction band bottom edge. Upon adsorption of carboxylated sensitizers on these acidic sites, coordination of Ti^{4+} surface ions by the dye's anchor provides sufficient electron density to raise the trap energy back to the conduction band edge level.

Rate constants for electron transfer from colloidal TiO_2 particles to dimethylviologen in aqueous solution were found to be strongly affected by surface states [3], the presence of traps causing the rate to decrease strongly. The pseudo-first order rate constant was 30 s^{-1} with bare TiO_2 at $pH = 3.6$, but jumped to 7×10^5 s^{-1} with adsorbed salicylate at $pH = 6$, due to the sweeping away of the traps into the conduction band by coordination of the adsorbate [3]. In nanocrystalline electrodes at $\phi_F < \phi_{cb}$, with species attached by a carboxylate or a phosphonate group, the surface has less traps. Though, trap sites located in the bulk of the solid, due in particular to oxygen vacancies

$|O|^+/|O|^0$ and $|O|^{++}/|O|^+$, are not affected by the derivatization of the surface and could still play an important role in affecting the kinetics of charge transfer from the conduction band to an acceptor across the interface.

11.2.2 Dye sensitizer

Many studies based on the observed bulk photoelectrochemical effects and on direct optical probing of the processes occurring at the solid surface have provided evidences that the sensitizing mechanism involves as a primary step electron or hole injection by the electronically excited sensitizer molecule into the semiconductor. Alternatively, charge injection can involve the reductive or oxidative quenching of the dye excited state by a redox active species (a *supersensitizer*), followed by thermal interfacial electron transfer :

$$S^* \mid SC + D \rightarrow S^- \mid SC + D^+ \rightarrow S \mid e^-_{cb}\,(SC) + D^+ \qquad (11.11)$$

$$S^* \mid SC + A \rightarrow S^+ \mid SC + A^- \rightarrow S \mid h^+_{vb}\,(SC) + A^- \qquad (11.12)$$

In the case of the injection of an electron from the excited state of a molecular sensitizer into the conduction band of a semiconductor (Eq. 11.2), the photoredox reaction thermodynamics requires the oxidation potential of the dye excited state $\phi^0\,(S^+/S^*)$ to be more negative than the flatband potential of the semiconductor ($\phi_{fb} = \phi_{cb}$ for minute-size particles), and thus :

$$\phi^0\,(S^+/S) < \phi_{cb} + \Delta E_{0,0} / \mathcal{F} \qquad (11.13)$$

where $\phi^0\,(S^+/S)$ is the oxidation potential of the dye, $\Delta E_{0,0}$ its excitation energy, $\phi_{cb}\,(SC)$ the conduction band edge potential of the semiconductor, and $\mathcal{F}$ the Faraday constant.

Provided the electronic coupling between the excited state of a dye sensitizer and localized acceptor states at the surface of the solid is sufficient, direct electron injection into trap sites is possible. This process was investigated in particular with alizarin dye anchored on the insulating substrate ZrO_2. Since the conduction band edge of zirconia lies about 1 eV above the singlet excited state of alizarin, electron injection into this band is not thermodynamically feasible. In spite of this fact, spectroscopic investigations have shown that on a femtosecond time scale the formation of the alizarin cation can be observed as a result of the electron injection into surface trap states [32]. The ultrafast injection dynamics into the traps observed in this system underlines the importance of surface states for the initial charge separation also for materials with lower band edge such as titanium dioxide.

The redox potential of the dye can shift upon adsorption from solution due to Coulombic or stronger covalent interactions with the solid substrate. This potential change can amount to several hundreds of millivolts. The oxidation potential and excitation energy of the fully protonated form of *cis*-$[Ru^{II}(dcbpyH_2)_2(NCS)_2]$ complex dye (N-3) in solution being ϕ^0 (S^+/S) = + 1.10 V/ SHE and $\Delta E_{0,0}$ = 1.65 eV, respectively, the oxidation potential of the MLCT excited state of the sensitizer establishes at ϕ^0 (S^+/S^*) = – 0.55 V/ SHE [33]. The flatband potential of TiO_2 in dry aprotic solvents can be as negative as ϕ_{fb} = – 1.25 V/ SHE [31,34]. In such conditions, the conduction band of the solid would in principle be out of reach of the dye excited state and only deep localized sub-bandgap states could potentially act as acceptor levels in the injection process. Surface protonation via adsorption of the carboxylic groups results however in a positive shift of the flatband potential that can amount to several hundred millivolts. Moreover, complete deprotonation of the four carboxylic groups of N-3 was demonstrated to cause its oxidation potential to shift negatively by *ca* 300 mV [35]. Both effects combined together with the presence of traces of H_2O render the interfacial electron transfer from the dye's excited state into TiO_2 thermodynamically favorable.

Figure 11.7 shows the potential bias dependence on the injection quantum yield from photo-excited $Ru(dcbpy)_3^{2+}$ into a TiO_2 nanocrystalline film. The luminescence of the surface-adsorbed dye was found to be strongly affected by the bias voltage applied to the oxide electrode [29]. At + 0.2 V, practically no emission could be detected, due to the oxidative quenching of the excited state by charge injection. Biasing the potential cathodically turned the typical luminescence of $Ru^{II}L_3$ gradually on, while the quantum yield of charge injection was observed to drop from 1 to 0.5. This effect was ascribed to the filling of the electronic states of the conduction band, leading to the increase of the energy of the lowest unoccupied levels. Biasing of the TiO_2 film can also result in the desorption of the sensitizer from the surface and to decreased injection yield [36].

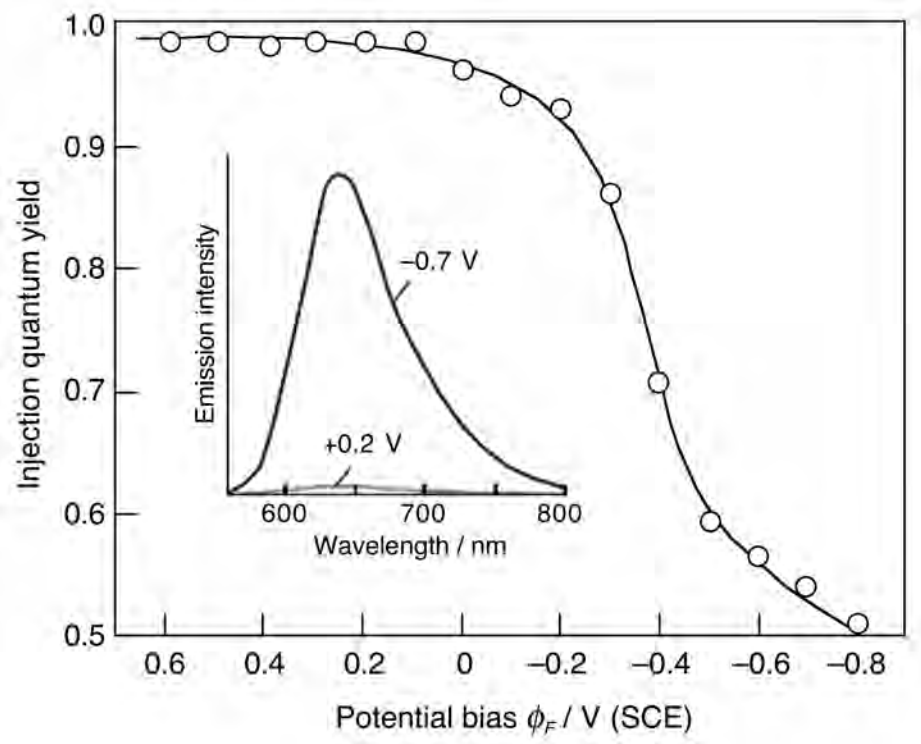

Figure 11.7 Effect of the potential bias on the apparent quantum yield of the electron injection from the excited $Ru^{II}(dcbpy)_3$ to the conduction band of TiO_2 [29]. The insert displays the luminescence spectra of the dye adsorbed on the surface of the mesoporous semiconducting film at two different potentials. Excitation wavelength is $\lambda = 500$ nm. The oxide electrode was immersed in aqueous 0.2 M $LiClO_4$ electrolyte at pH 3.

11.3 KINETICS OF INTERFACIAL ELECTRON TRANSFER

11.3.1 Charge injection dynamics

The standard theoretical treatment for molecular electron transfer (ET) was provided by Marcus supplying a correlation of the difference in Gibb's free energy ΔG between donor and acceptor, the curvature of the potential surfaces and the reorganization energy. Within the framework of Marcus theory, ET rates for many systems could be predicted quite well and further quantum mechanical extensions were even able to increase the area of validity. All of these electron transfer theories are based on the assumption that the vibronic coupling is strong and that ET is controlled by nuclear motion. Tunneling between the electron donor and the acceptor states occurs when both electronic levels are made resonant by energy fluctuations caused by the surrounding thermal bath. The situation can be illustrated by an energy scheme (Fig. 11.8, left), showing the situation for an ET-reaction between a donor (D) and an acceptor species (A). In a classical view, the system can propagate along a generalized reaction coordinate on the potential energy surface (PES) of the electronic configuration, approximated as one-dimensional parabola. Energy conservation allows an electronic transition between the initial encounter complex D–A (i) and the final charge separated state $D^+ A^-$ (f) only at the intersection of the two PESs, where the electron can be transferred from D to A. In the configuration where donor and acceptor levels have the same energy, exactly at the crossing point of the i and the f parabolas, electron transfer can occur with a certain probability, depending on the electronic coupling matrix element between the initial state D–A and the final charge separated state $D^+ A^-$. Based on this microscopic view of electron transfer, macroscopic rates can be calculated by assuming a thermal occupation of the energy eigenstates of the D–A potential, the electron transfer process being mediated by molecular vibrations [37,38].

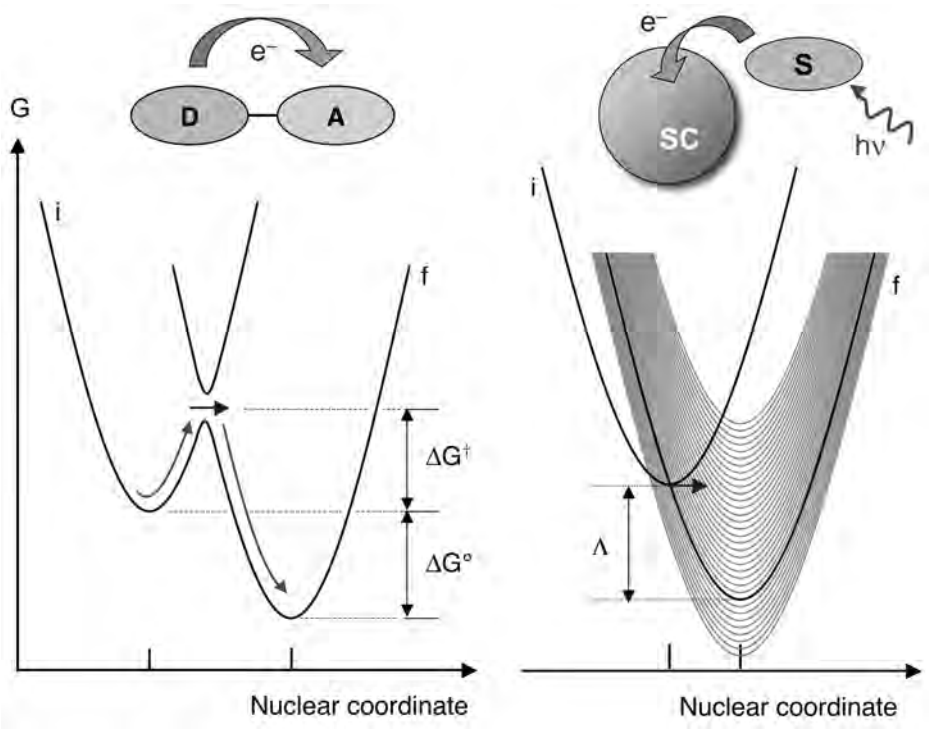

Figure 11.8 Energetic situation for a typical vibration-mediated electron transfer between a donor (D) and an acceptor (A) described by Marcus theory (left) and the situation prevailing in the case of a continuum of acceptor states found in the dye-sensitization of a semiconductor (right).

A fundamentally different situation for electron transfer is found in dye/ semiconductor systems under illumination. Figure 11.8 (right) shows a schematic of such a system. The acceptor level in this case is the energetically broad conduction band of the semiconductor (SC). As a consequence, the final charge-separated state energy surface splits up into a manifold of acceptor parabolas and each point of the reactant parabola is a transition state. In this wide-band limit case, there is no need of an energy matching mechanism via molecular vibrations and the rate constant for interfacial ET is essentially independent of nuclear factors. The only remaining parameter determining the injection rate is the electronic coupling, representing the electronic overlap integral between donor and acceptor states [37,38].

The simplest kinetic model describing the charge injection as a non-adiabatic radiationless process is derived from Fermi's golden rule. The rate constant for the reaction can then be expressed as the product of a Franck-Condon weighted density of states (*FCWD)*, which depends on the driving force ΔG^0 as well as the nuclear reorganization energy Λ accompanying the electron transfer, and an electronic factor which is proportional to the electronic coupling matrix element $|H|$ squared :

$$k_{et} = \frac{2\pi}{\hbar} |H|^2 \, FCWD \tag{11.14}$$

The *FCWD* is the integrated overlap of reactant and product nuclear wavefunctions of equal energy. For a large number of accessible acceptor levels, the summation over all the terms of the *FCWD* factor reduces to a pure density of final electronic states [37]. The rate constant k_{inj} of the charge injection process can therefore be expressed by :

$$k_{inj} = \frac{2\pi}{\hbar} |H|^2 \rho \;\; \cong \;\; \frac{2\pi}{\hbar} |H|^2 \frac{1}{h\omega} \, n_a \tag{11.15}$$

Here k_{inj} is the first order rate constant for interfacial charge transfer from a single reactant level to a continuum of electronic product states with density of states ρ and constant electronic coupling $|H|$ to all product states. The actual density of final states ρ can be approximated by the reciprocal energy level spacing $1/h\omega$ of the dye cation oscillator of frequency ω, multiplied by a factor $0 < n_a < 1$ accounting for the density of empty electronic states available in the solid. Above the flatband energy level, the density of acceptor states in the conduction band of a semiconductor is usually very large and the density of final states ρ solely determined by the density of energy levels of the dye cation ($n_a \cong 1$). Below the band edge, empty trap states are present, whose density decreases gradually at lower energies ($n_a \rightarrow 0$).

The density of accepting states $N_c(E)$ in the conduction band of a semiconductor at the energy level E is given by equation 11.16 [39]:

$$N_C(E) = 4\pi \left(\frac{2m_{de}^*}{h^2} \right)^{3/2} (E - E_{cb})^{1/2} \qquad (11.16)$$

where E_{cb} is the energy of the conduction band bottom edge, and m_{de}^* the density-of-state effective mass for electrons. The latter parameter depends strongly on the material. In TiO_2, for instance, $m_{de}^* \cong m_e^* \geq 6\, m_e$ (where m_e is the electron rest mass) and the calculated density of states at least two orders of magnitude larger than that in ZnO, in which $m_{de}^* \cong 0.24\, m_e$ [40,41]. The density of states is also expected to be dependant upon the size of the semiconductor nanocrystallites. Strong quantum confinement indeed results in widely spaced electronic levels and therefore in a very low density of states. Although this size quantization effect would be negligible for TiO_2 where the exciton binding energy is very small, it is expected to play a significant role for ZnO particles whose diameter is smaller than ~10 nm.

Equation 11.15 can only be used when the electron transfer process takes place from a single prepared excited state of the sensitizer. In the general case, absorption of photons, whose energy $h\nu$ is larger than the electronic excitation energy $\Delta E_{0,0}$ of the dye, leads to the population of higher vibronic levels of the molecule. Relaxation of these vibrationally excited intramolecular states and of the whole system along the classical reaction coordinate is expected to compete with the electron transfer process. In these conditions, the electronic coupling $|H|$ between the donor and the acceptor states becomes a time- and excitation wavelength-dependant function and cannot be readily accessed anymore [38]. Figure 11.9 illustrates the competition between fast electron transfer from an excited vibronic level of the initial (i) state to the final (f) state and relaxation to the lower vibrational level of the reactant. In principle, each crossing

point at which ET occurs corresponds to a different value of the electronic coupling matrix element $|H|$. If a normal Marcus region situation prevails ($-\Delta G_{et}^{0} \leq \Lambda$), vibrational relaxation of the electronic excitation state results in increased activation energy for the reaction. Hence, charge injection from hot vibronic states of a sensitizer is usually kinetically more favorable than ET from the lower vibrational level of the reactant state.

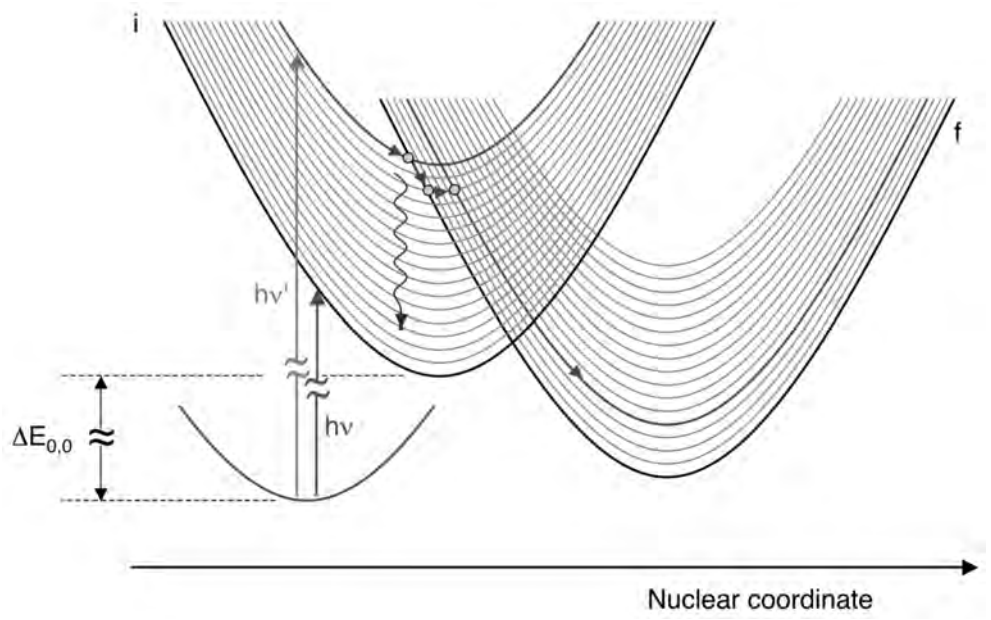

Figure 11.9 Illustration of the competition between fast electron transfer from hot vibronic levels of a sensitizer and its vibrational relaxation. ET from the initial vibronic state prepared by absorption of radiation energy hν' has a smaller activation barrier than that excited by energy photons hν or obtained after vibrational relaxation to the lower level of the reactant state.

Two limiting cases could be considered that would, however, let us treat in a simple way the interfacial electron transfer process as involving a single prepared excited state of the sensitizer: (a) Charge injection is slow enough compared to the vibrational relaxation of the dye excited state. In this event, electron transfer would be able to take place only from the lowest excited state, and the injection quantum yield

would be simply controlled by the kinetic competition between the electron injection and the decay of the excited state. (b) Charge injection is fast compared to nuclear relaxation of the excited state. In this case, interfacial charge transfer would take place from the prepared hot vibronic level and the quantum yield for the primary injection process would be close to unity. For both limiting cases, Eq. 11.15 would be relevant, provided electron transfer is non-adiabatic.

When the electronic coupling of the donor and acceptor becomes sufficiently large (typically $|H| > 150\ \mathrm{cm}^{-1} \cong 0.7\ k_B T$), the electron transfer will be increasingly adiabatic and, in the absence of solvent dynamics control, the rate constant will eventually be proportional to a nuclear vibration frequency ω_n. In this case the electronic coupling element does not enter into the rate expression. For other cases, where $|H|$ is small enough, the value of the coupling element is needed for a quantitative description of the electron transfer rate. There is obviously a considerable interest in the role of the electronic coupling factor, as the separation distance and anchoring geometry of the sensitizer on the surface will determine its magnitude. The Gamov expression (Eq. 11.17) is used to estimate the changes in $|H|$ in photoinduced electron transfer, where the electron donor and acceptor are separated by a fixed distance r :

$$|H|^2 = |H|_0^2 \exp\left[-\beta\,(r - r_0)\right] \tag{11.17}$$

The damping factor β is an exponential coefficient for the decay of the electronic wavefunction and has typically values ranging from 0.2 to 2.5 Å^{-1}. Provided that other factors do not influence the electron transfer rate, Eq. 11.18 can be used to estimate the rate at a known separation distance :

$$k_{et} = k_{et}^0 \exp\left[-\beta\,(r - r_0)\right] \tag{11.18}$$

Other parameters, such as spin changes, symmetry factors, and the relative orientation of both reactants may obviously also influence the magnitude of the electronic coupling factor $|H|^2$.

Determining injection rates experimentally

Most of the previous knowledge on bulk semiconductor-electrolyte interfacial charge transfer is derived from steady-state photocurrent measurements achieved in photo-electrochemical cells. Obtaining electron transfer rate constants from such an indirect method, however, is difficult because photocurrent depends on many other interfacial and bulk processes. The rapid dynamics of electron injection can be investigated by application of transient laser spectroscopy to colloidal dispersions or nanocrystalline semiconductor films. Such materials are particularly amenable to time resolved optical studies, as they display a good transparency throughout all the visible and NIR spectral domains. Moreover, they are characterized by a large surface area exposed to the solution, yielding high sensitizer absorbance for only monolayer dye coverage. Most presently studied oxide semiconductor systems, namely TiO_2, SnO_2 and ZnO, are of particular interest for the development of artificial photosynthetic and photovoltaic devices.

Earlier studies on dye sensitized titanium dioxide reported nanosecond time constants for the injection kinetics in aqueous medium [42-44]. These results were obtained indirectly from the measurement of the injection quantum yield and implicitly assumed that the interfacial electron transfer reaction was competing only with the decay of the dye excited state. More recent studies were based on the same assumption, but used measurements of the dye emission lifetime, which provided ns - fs time resolution [45-48].

Direct time-resolved observation of the build up of the optical absorption due to the oxidized dye species S^+ has been employed in most of the recent studies. This appears as a more reliable way of monitoring the charge injection process, as it does not require any initial assumption on the sensitizing mechanism and is not sensitive to the self-quenching of the dye excited state. A powerful approach is constituted by the direct detection by ultrafast mid-IR spectroscopy of injected electrons in the conduction band and in sub-band states. Using the same technique, vibrational spectra of transient molecular species deriving from the adsorbed sensitizer can in principle also be recorded [41].

Various molecular sensitizers have been investigated in conjunction with metal oxides. Organic dyes, like xanthenes, phosphonated perylene and carboxylated anthracene, coumarin-343, porphyrins, anthraquinones and natural anthocyanines were employed as model systems. A majority of photo-induced charge injection dynamics studies relevant to efficient DSCs have, however, used ruthenium(II) polypyridyl complexes, and more particularly [*cis*-$Ru^{II}(dcbpyH_2)_2(NCS)_2$] (N-3), or its partially deprotonated form [*cis*-$Ru^{II}(dcbpyH)_2NCS)_2]^{2-}$ (N-719). The choice of the latter compound has been principally motivated by its success as a very efficient dye-sensitizer in molecular photovoltaic cells. Upon irradiation by visible light, adsorbed N-3 and N-719 dyes has been found to inject electrons into TiO_2 nanocrystalline electrodes with a quantum yield approaching unity [33]. Newly developed push-pull organic dye sensitizers recently displayed remarkable spectral properties and stability, which make them credible competitors of Ru(II) polypyridyl complexes. These compounds are typically equipped with a cyanoacrylate group, serving simultaneously as an acceptor carrying the LUMO of the molecule and as an anchor to the oxide surface, a thiophene bridge and a triarylamine donor moiety [49-51]. Ultrafast laser flash photolysis was applied to dye-sensitized transparent films, the results of which will be used here as an example to illustrate the dynamics of the injection process.

Example of $[Ru^{II}(dcbpy)_2(NCS)_2]$-sensitized titanium dioxide

Figure 11.10a shows the transient difference spectra obtained upon nanosecond laser excitation of N-3 in ethanolic solution and of nanocrystalline titanium dioxide transparent films, onto which the sensitizer was adsorbed. The dye is excited with $\lambda = 605$ nm output of a laser system and the absorbance change observed immediately after the laser excitation is plotted as a function of the detection wavelength [52]. Luminescence quenching and photocurrent experiments have confirmed that $\lambda = 600$ nm excitation of the sensitizer resulted in the formation of the charge separated state $S^+ | e^-_{cb}$ (SC). The spectrum obtained upon irradiation of dye sensitized TiO_2 displays a broad absorption feature peaking around 800 nm, which half-lifetime exceeds 0.5 μs. Such a lifetime is more than one order of magnitude longer than that of the isolated dye excited state in solution ($\tau \cong$ 15-50 ns) [33]. The recorded spectrum is comparable to that of the one-electron oxidation product $[Ru^{III}(dcbpy)_2(NCS)_2]^+$ of the complex produced by oxidative quenching of the excited state in an alcoholic solution containing methylviologen as an acceptor [53], or generated by pulse radiolysis [54]. It can be readily distinguished from the spectrum of the dye excited state obtained in solution, whose band maximum is located at $\lambda = 710$ nm. These observations demonstrate unambiguously that the transient spectral feature observed upon excitation of the sensitized semiconductor cannot be assigned to an excited state of the dye but must be attributed to the charge separated state resulting from interfacial charge injection, where both a LMCT transition of the -NCS ligands to the Ru(III) metal ion center in S^+ and absorption by conduction band and/or trapped electrons contribute to the spectrum.

Further sub-picosecond data were collected. Transient data measured for dye-sensitized TiO_2 films were compared with those obtained for control dye-coated ZrO_2 films, as the high conduction band edge of the latter material should prevent electron injection. Figure 11.10b shows the absorption difference spectra obtained at a time delay

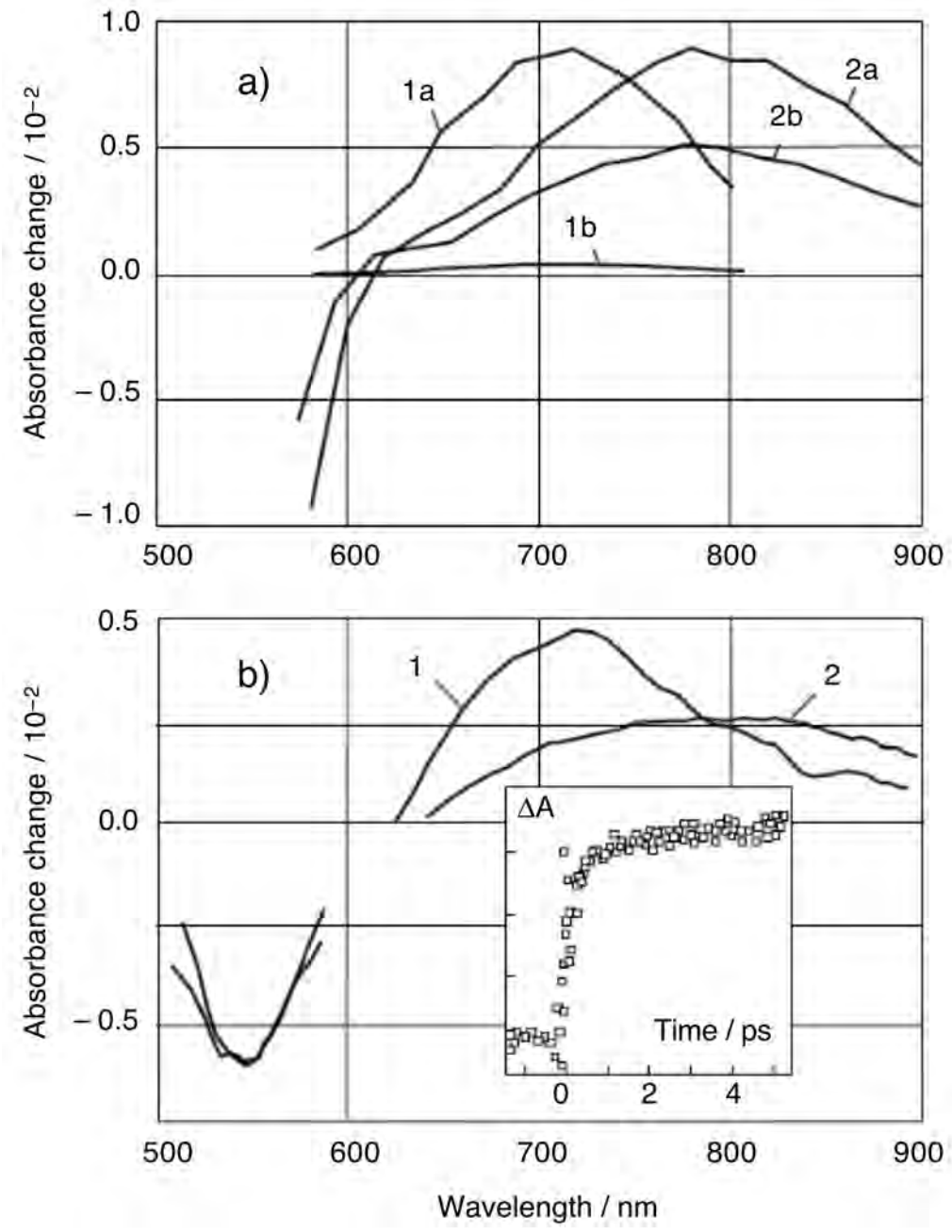

Figure 11.10 a) Transient absorbance spectra obtained upon ns pulsed laser excitation of N-3 dye in ethanol (1) and adsorbed on a TiO_2 transparent film (2). Spectra were recorded 50 ns (1a, 2a) after laser excitation ($\lambda = 605$ nm, 5 ns pulse duration). b) Transient absorbance spectra recorded 6 ps after ultrafast laser excitation ($\lambda = 605$ nm, 150 fs pulse duration) of N-3 dye in ethanol (1) and a freshly sensitized TiO_2 film (2). The insert shows the temporal behavior of the absorbance of N-3 | TiO_2 measured at $\lambda = 750$ nm with sub-ps time resolution.

of 5 ps after $\lambda = 605$ nm pulsed excitation. The spectrum obtained for the dye-sensitized zirconia films exhibits a maximum at 710 nm as observed for the N-3 dye in ethanolic solution and is therefore assigned to the dye MLCT excited state. On the other hand, the transient spectrum recorded for sensitized TiO_2 displays a maximum at 800 nm that is characteristic of the dye cation. In contrast to the data obtained for dye-coated ZrO_2 films, the difference spectra measured with sensitized TiO_2 exhibited some temporal evolution for time delays less than 5 ps. Typical transient absorption data at a probe wavelength of $\lambda = 750$ nm is shown in the insert of Figure 11.10. The data show a fast ~100 fs instrument response limited signal growth followed by a slower kinetic phase extending on several picoseconds. A detailed multi-exponential analysis of the traces obtained revealed at least three kinetic components with lifetimes of <100 fs (35 %), 1.3 ps (22 %) and 13 ps (43 %) [34,55].

Non-exponential injection dynamics

The kinetics of the electron injection from N-3 have been under active study for the last decade [48,53,56-60]. Some studies conducted with the same system in somehow slightly different conditions report only a single < 50 fs phase of electron injection [41,45,56,60]. After the seminal work of Tachibana et al. [53], who reported the charge injection to take place within < 150 fs (50%) and 1.2 ps (50%), the study by Benkö et al. also found the electron transfer to occur in a biphasic way [57]. A first, ultrafast component was estimated to have a rise time of 28 fs and a second, multiexponential part occurred in the 1-50 ps time domain. Although most of other recent studies seem to confirm the presence of the slower kinetic component, the relative contribution of the latter ranges throughout the literature from 16 to 65 % and the time constants vary from 0.7 to 100 ps with a marked non-exponential behavior. This discrepancy between reported results is illustrated by Figure 11.11. Lately, time-resolved single photon counting was used to measure the electron injection dynamics in complete DSCs

employing N-719 ruthenium bipyridyl sensitizer. While the quenching of *ca* 50% of the dye's triplet state photoemission could not be time-resolved, 50% of the excited states appeared to decay with a half time of 200 ps [48,61] .

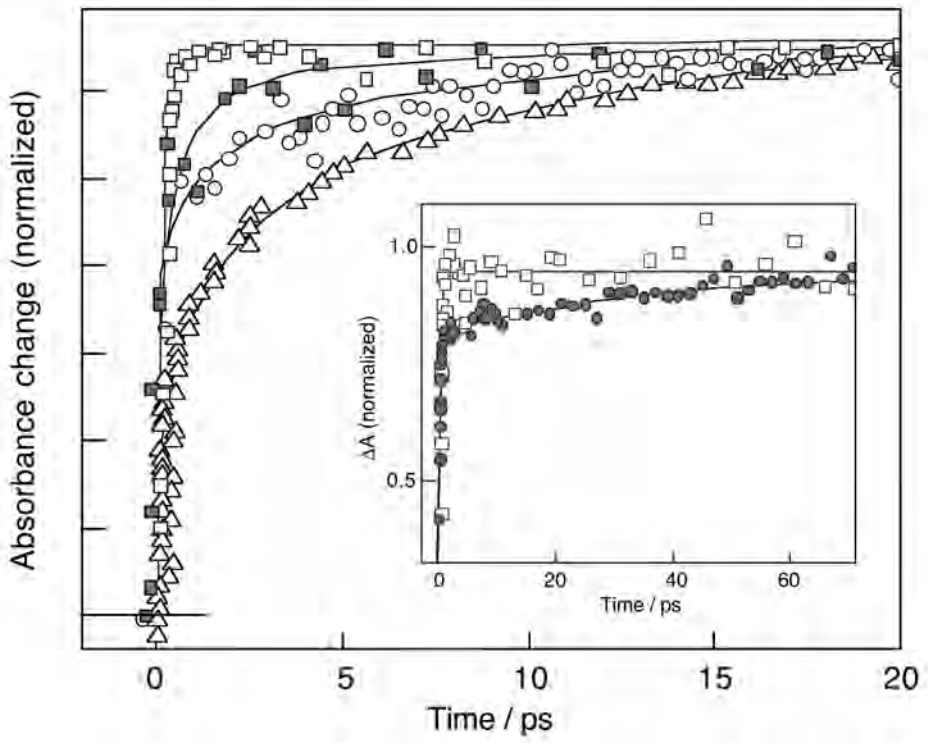

Figure 11.11 Transient absorbance signals recorded after ultrafast excitation of N-3 dye adsorbed on nanocrystalline TiO_2 at probe wavelengths $\lambda = 860$ nm (□) [60], 1.6 μm (■) [58], 760 nm (○) [34], and 860 nm (△) [59] as reported by four different research groups. In all cases, the temporal evolution of the signal, due to absorption by oxidized dye species S^+ and/or conduction band electrons, provides a direct measurement of the kinetics of the same charge injection process. The insert shows the effect on the observed kinetics of the concentration of the ethanolic dye sensitizer solution used to load the oxide surface: 0.3 mM (□) and 0.015 mM (●) [60].

The observed intricate injection kinetics was rationalized by Sundström et al. in terms of a two-state mechanism, the fast and slow components being attributed to the injection from the singlet and the triplet excited states of the ruthenium complex,

respectively [57]. Other authors attribute the multiphasic nature of the injection to sensitizers adsorbed on energetically different sites or in various spatial configurations at the surface of the mesoscopic titania films [62]. The origin of such a complex electron transfer kinetics is not clear yet. The large spread of time constants experimentally determined for the injection process and the obvious contradictions between data reported in the literature put in question the proposed interpretations. The participation of various singlet electronic excited states of the Ru(II) complex to the reaction is ruled out as one fails to observe any effect of the excitation wavelength. Nor was a significant difference observed in the results obtained for dyed TiO_2 films exposed to air and in propylene carbonate, thus apparently excluding possible effects due to the solvation dynamics. Direct interfacial electron transfer to various localized defect states could be associated to different electronic coupling elements and could therefore result in a wide distribution of rate constants. The occupancy of these trap states can be modulated by sweeping the Fermi level below the flatband energy upon applying an external electrical bias. Modulation of the applied potential, does not appear, however, to result in any noticeable change in the injection yield and fast kinetics [34]. On the other hand, adsorption of potential determining cations, such as Li^+, that causes the flatband potential of the semiconductor to shift positively, apparently affect the electron injection rate [34,63]. These observations suggest that the multiple time constants result from heterogeneities in the energetics of the nanocrystalline TiO_2 films.

Effect of surface dye coverage on the injection kinetics

Adsorption of dye molecules on different surface sites and with various anchoring geometries could also cause an intricate kinetic outcome [60,64]. Results obtained with eosin-sensitized aqueous TiO_2 colloids showed that kinetic heterogeneity could arise from intermolecular interactions and a wide distribution of geometrical conformations of loosely bound dye molecules on the surface [6]. By carefully controlling the

deposition of N-3, N-719 and of their parent heteroleptic [Ru^{II}(4,4'-dicarboxylic)(4,4'-dinonyl-2,2'-bipyridine)$(NCS)_2$] (Z-907) complex onto nanocrystalline TiO_2, oxide films sensitized by much less than one dye monolayer display essentially a monophasic injection kinetics with a time constant of less than 20 fs [60]. On the other extreme, adsorption of the sensitizer on the oxide surface for a prolonged time or from concentrated dye solutions leads to a marked decrease of the initial rapid phase and to the appearance of slower kinetic components. These extend to tens of picoseconds and account for up to 26 % of the overall number of S^+ species formed during the injection process (Fig. 11.11, insert). These results show that the slow kinetic phase observed for electron injection from N-3 or N-719 into TiO_2 is not an intrinsic property of the dyes as previously suggested. It is rather a consequence of aggregation and poor ordering on the semiconductor surface of dye molecules, whose electronic coupling with acceptor levels of the semiconductor is then reduced by orders of magnitude.

In the presence of high concentrations of iodide ($[I^-] \geq 0.8$ M) – a situation typically encountered in ionic liquids based on iodide melts where I^- concentration can reach 6 M – significant reductive quenching was observed for aggregated samples. Up to 25 % of the dye excited states were intercepted in these conditions before they could inject [65]. Reaction of aggregated dye excited states with iodide appeared to take place within a few tens of ps. As well, N-719 and Z-907 anions formed by reductive quenching of loosely bound dye excited states on the surface were found to be extremely long-lived and to decay with a time constant of ca. 1 ms. Despite the large thermodynamic driving force for charge injection from dye anions into the semiconductor conduction band, this reaction does appear then to take place. This means that a non-negligible fraction of the potential photocurrent could be lost in DSCs through the reductive quenching route in the presence of high iodide contents. The mechanism of the one-electron oxidation of I^- by the dye excited state S* or by the oxidized species is believed to be similar and will be discussed in section 11.4.1.

Injection from hot vibronic excited states of the dye

There is now compelling evidence that the fastest kinetic phase of electron injection in *cis*-[$Ru^{II}(dcbpy)_2(NCS)_2$]-sensitized nanocrystalline titanium dioxide films takes place in the femtosecond regime. The vibrational relaxation of the dye excited state, on the other hand, is expected to occur typically within 0.4–1 ps ($k_v \cong 10^{12}$ s^{-1}). Observed injection rate constants of the order of $k_i = 10^{13}$-10^{14} s^{-1} therefore certainly preclude thermalization of the dye excited state S* to its lowest vibrational level $v' = 0$ prior to the reaction, and suggest that charge transfer can occur directly from hot ($v' > 0$) excited sensitizer molecules. To experimentally test this possibility, systems were designed in such a way that the $v' = 0$ energy level of the electronically excited state of the dye lies below the bottom of the conduction band of the semiconductor, where the density of available acceptor states is low (Fig. 11.12). In these conditions, charge injection from vibrationally relaxed excited molecules of the sensitizer is either slow or unfeasible. However, when electron injection from a hot vibronic state of the dye is able to compete successfully with its nuclear relaxation ($k_i' > k_v$), charge injection becomes possible for higher excitation photon energy, and an excitation wavelength dependence of the quantum yield $\Phi_i = k_i' / (k_i' + k_v)$ is obtained [52,66,67].

Whether hot injection could eventually lead to a practical device system allowing to exceed the single-junction Shockley-Queisser limit of 31 % for photovoltaic power conversion efficiency is debatable [2]. Collection of hot conduction band electrons before their thermalization and trapping seems indeed to be more difficult to realize than hot injection from upper vibrational levels of electronically excited molecular sensitizers.

Observations of an excitation wavelength dependence of the charge injection process show that photoinduced interfacial electron transfer from a molecular excited state to a continuum of acceptor levels can take place in competition with the relaxation

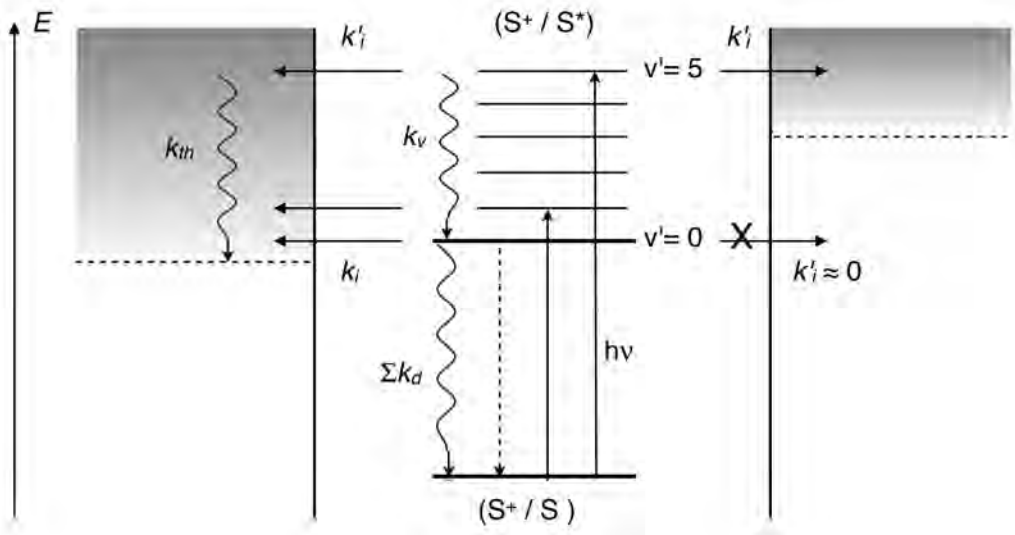

Figure 11.12 Energy scheme for a dye sensitizer S adsorbed on semiconductors characterized by different values of E_{cb}. On the left, charge injection is thermodynamically feasible for the dye excited by photons of any energy $h\nu \geq \Delta E_{0,0}$. In the situation depicted on the right, only photoexcitation to hot energy states ($h\nu > \Delta E_{0,3}$) allow for the injection process.

from upper excited levels. The rather slow growth of the injection quantum yield above the energy onset suggests it actually reflects the density of acceptor states in the solid that are present below the conduction band edge. In conditions where the injection quantum yield is unity ($k_i' >> k_v$) and electron transfer takes place to the conduction band of the semiconductor ($n_a \cong 1$), the occurrence of the electron transfer process from a single prepared state S*($v' > 0$) validates the simple model of Eq. 11.15 and allows to estimate the electronic coupling matrix element $|H|$. Assuming a frequency of the dye cation oscillator $\varpi \leq 1500$ cm^{-1}, a value of $|H| > 500$ cm^{-1} ($\cong 2$ kT) would be calculated from a rate constant $k_i = 5 \cdot 10^{13}$ s^{-1} measured typically for [Ru^{II}(dcbpy)$_2$(NCS)$_2$]-sensitized nanocrystalline TiO_2. Although the value used for the cation vibration frequency ϖ, and therefore that determined for $|H|$, are here probably over-estimated, this figure corresponds to a rather strong electronic coupling and suggests the electron injection rate has reached the adiabatic limit.

Parameters influencing the rate of electron injection

The Franck-Condon weighted density of states factor, that comprises parameters such as the reaction free energy ΔG^o, the nuclear reorganization energy Λ and the temperature T, is expected to play only a negligible role in systems that are kinetically near optimum in terms of the Marcus theory and that are characterized by a large number of acceptor states. According to Eq. 11.14, the rate of interfacial electron transfer is controlled only by the electronic coupling matrix element $|H|$ and the acceptor states density. The activationless nature of the charge transfer process has been experimentally confirmed by the observation of temperature independent injection kinetics [68]. Other reported data show that, in energetically favorable conditions, the rate of electron injection is not controlled by the energetics of the sensitizer's excited state, nor by the medium reorganization, but rather by the density and occupancy of electronic states in the solid [34].

The rate of electron injection in nanocrystalline ZnO and MoS_2 quantum dots has been measured. In *cis*-[$Ru^{II}(dcbpy)_2(NCS)_2$]-sensitized zinc oxide, a highly non-exponential injection kinetics was measured that could be fitted by three exponential components with < 1 ps (18 %), 42 ps (46 %), and 450 ps (36 %) rise times [69]. The multi-exponential kinetics could be described by a model assuming a Gaussian distribution of electronic coupling between the π* orbital of the ruthenium complex ligands and the accepting orbitals in the solid. The observed kinetics is about 10–100 times slower than that measured on TiO_2 in similar conditions. This important difference can be rationalized by the density of states in the conduction band of ZnO, which is estimated to be about two orders of magnitude smaller than that in titanium dioxide [11]. In small MoS_2 nanoclusters, an electron injection time of 250 ps was observed upon sensitization by N-3 dye [64]. Ground state spectra and adsorption properties of the dye suggested in this case that electronic coupling between the carboxylated ligands and the semiconductor surface could not be very different from

that on TiO_2 and ZnO. The quite slow kinetics observed on MoS_2 is therefore likely to be the result of a far smaller density of acceptor states in nanoclusters that exhibit a strong quantum-confinement.

On titanium dioxide, the photoinduced charge injection process was reported to take place on time scales ranging from less than 10 fs to several microseconds, depending on the sensitizer and conditions used [70]. Such a spread of the values of k_i over nine orders of magnitude can be accounted for only by very different values of the electronic coupling between the dye excited state and the acceptor orbitals at the surface of the semiconductor. Using Eq. 11.15, and assuming for all systems $n_a = 1$ and an average collective vibrational mode frequency of the dye oxidized state $\varpi = 1500\ \text{cm}^{-1}$, electronic coupling matrix element can be calculated for each sensitizer. Obtained values of $|H|$ vary from 0.02 cm^{-1} to > 1600 cm^{-1}. $|H|$ values > 200 cm^{-1} ($= k_B T$) are however hardly compatible with the non-adiabatic assumption of Fermi's golden rule (Eq. 11.14) and injection processes occurring in less than 50 fs should then be considered to proceed adiabatically. Considering Eq. 11.17, and assuming a through-space damping factor $\beta = 1.2\ \text{Å}^{-1}$, the full range of k_i figures between $2 \cdot 10^5\ \text{s}^{-1}$ and $2 \cdot 10^{13}\ \text{s}^{-1}$ implies a difference in the electron transfer reaction distance of the order of 15 Å between the slowest and the fastest system.

Various types of association of the sensitizer with the oxide surface could explain such a difference. The strong electronic coupling prevailing for an efficient sensitizer is generally the result of the anchoring of the dye molecule onto the semiconductor surface through a moiety carrying its lowest unoccupied molecular orbital (LUMO). This situation is clearly encountered in carboxylated Ru(II) polypyridyl complexes, coumarin or alizarin dyes. The examples provided by xanthenes and N-3 dye-sensitization of titanium dioxide demonstrate that the mode and geometry of adsorption of sensitizers at the surface of the semiconductor can strongly affect the ultrafast photoinduced charge injection dynamics. A decrease of the donor-acceptor electronic

coupling is likely to occur with dye molecules loosely associated to the semiconductor charged surface through electrostatic interaction and/or hydrogen bonding. Results obtained for the eosin-sensitized aqueous titanium dioxide colloids are exemplary of the sensitivity of the dynamics of interfacial electron transfer upon surface and environmental conditions in the weak-coupling case [6]. Dispersion of dye monomers within a nanometers-thick polyvinyl-alcohol adlayer yielded a broad distribution of distances separating the sensitizer's excited states from the reactive surface. In this situation, kinetic parameters for charge injection in the conduction band of TiO_2 were found to cover a large time span from typically 200 fs to hundreds of picoseconds, and were only limited at longer times by radiative and nonradiative decay of the dye excited states.

For Ru(II) bipyridyl sensitizers as well as organic dyes, strong electronic coupling between the π^* molecular orbital of the dye excited state and the empty Ti^{IV}-3d orbital manifold of the semiconductor is achieved by directly linking the sensitizer's moiety that carries the LUMO to the surface. Both carboxylic and phosphonic anchoring groups are quite good in attaching dye sensitizers onto the surface of TiO_2. Though, they are not equivalent in terms of electronic coupling. Carboxylic groups attached in the 4,4' position on bipyridyl ligands are conjugated with the π-system of the aromatic core. As a result, the LUMO carried by the ligands can extend through this conjugated bridge in close proximity to the first empty d-orbitals of surface Ti(IV) ions and thus ensure strong electronic coupling with the conduction band acceptor levels. π-conjugation is not possible through phosphonic groups, which act then as insulating bridges between the bipyridyl ligand and the surface. Although the adsorption equilibrium constant is larger for phosphonated ligands than for their carboxylic counter part, phosphonated dyes are characterized by weaker electronic coupling for charge injection. Figure 11.13 provides an illustration of the results obtained in the determination of the injection dynamics from two similar $Ru^{II}(tpy)(NCS)_3$ dyes, whose

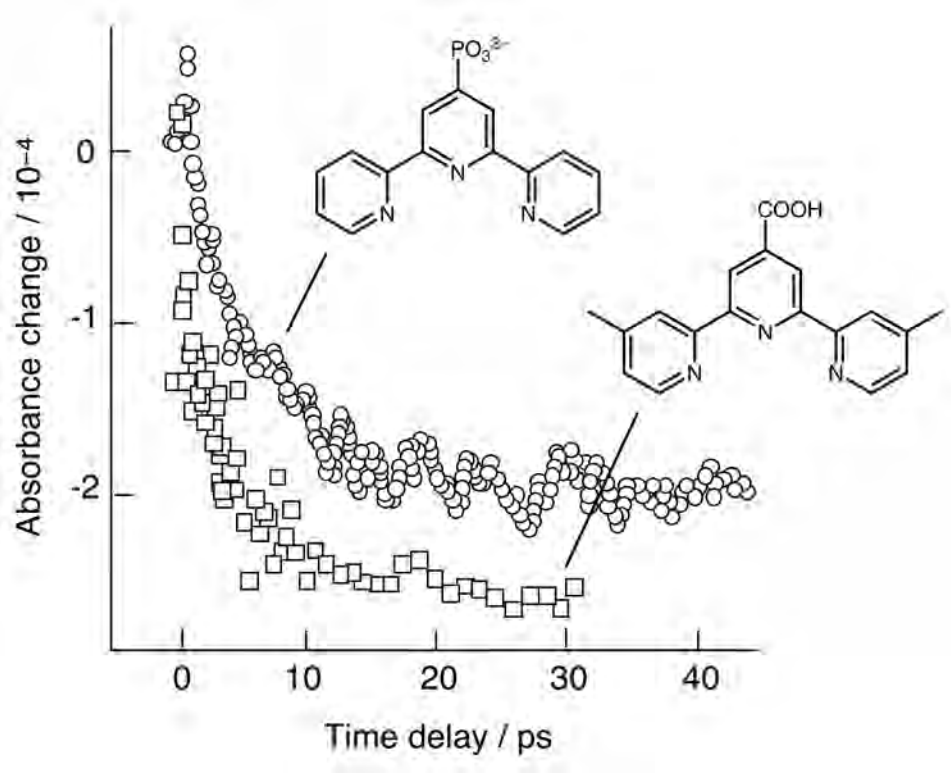

Figure 11.13 Ultrafast transient absorption data of $Ru^{II}L(NCS)_3 \mid TiO_2$ systems recorded with pump and probe wavelengths of 530 nm and 560 nm, respectively. The structure of the terpyridyl ligand L is indicated for each set of data. The absorbance change is due to the decay of the dye excited state during the electron injection process. The kinetics of the injection from the carboxylated dye can be fitted by time constants 120 fs (50%) and 800 fs (50%). Time constants for the phosphonated sensitizer are 800 fs (50%) and 17 ps (50%) [71].

terpyridyl ligand carries a single carboxylic and a phosphonic anchoring group, respectively. The rate constant obtained for the faster kinetic component is $k_i = 8.3 \cdot 10^{12}\ s^{-1}$ for the carboxylated compound and $k_i = 1.2 \cdot 10^{12}\ s^{-1}$ for the phosphonated sensitizer. Applying again Eq. 11.17 and assuming a distance damping factor $\beta = 1.0\ Å^{-1}$, this 7 fold difference corresponds to an increase of the distance for electron transfer by *ca* 2 Å, which is roughly equivalent to the dimension of the phosphonic group spacer.

The electronic coupling for interfacial ET can be diminished deliberately by increasing the distance separating the LUMO of the dye from the surface of the semiconductor material. The dependence of the multiphasic injection dynamics upon this parameter could serve to discriminate between the various possible sources of kinetic heterogeneity. This can be achieved, for instance, by inserting insulating spacer units between the chromophore and the anchoring group of the dye. Lian and co-workers have studied the bridge-length dependence of ultrafast charge injection from rhenium-polypyridyl complexes to TiO_2 and SnO_2 films and have suggested that the transition between the strong- (adiabatic) and weak coupling (non-adiabatic) cases takes place for transfer distances increased by only one $-CH_2$ unit length (~ 3 Å) [58,72]. The lengthening of the bridge spacer does not lead in all instances to slower kinetics, especially if the linker is too flexible or when the molecule can adopt a tilted orientation on the surface. In an attempt to circumvent this problem, rigid oligophenylene bridges [73,74] and tripodal linkers oxide [75] were synthesized to anchor sensitizers to the surface of semiconductor oxide. Sub-picosecond injection rate was observed over a distance of more than 20 Å, with apparent damping factor values of the order of $\beta = 0.04$ Å^{-1}, indicating important delocalization of the excited state over the rigid spacer arm [74,75]. Perylene-based tripodal sensitizers were studied in conjunction with other perylene sensitizers in ultra-high vacuum conditions [76]. Injection time constants ranging from 13 fs to 4 ps were measured and an exponential dependence upon ET distance was observed with a damping factor $\beta = 1$ Å^{-1}, compatible with through-space electronic tunneling.

The distance dependence was investigated by another mean using the phosphonated Ru^{II}(4'-PO_3-tpy)$(NCS)_3$ dye adsorbed on TiO_2 core particles coated by an insulating Al_2O_3 shell of increasing thickness. Experimental results displayed by Figure 11.14 show that electron injection occurs with a relatively high quantum yield for tunneling barriers as thick as 2-3 nm. Neglecting ultrafast injection, which is likely

to be due to dye molecules directly attached to TiO_2 from holes in the alumina layer, a biphasic injection kinetic was observed resulting again in $\beta = 0.04 - 0.11$ Å^{-1}. As the barrier to the conduction band of bulk, crystalline Al_2O_3 is very large (> 3 eV), a β value of approximately 1 Å^{-1} was expected. In nm-sized layers made of amorphous aluminium oxide, empty states should however exist at a potential of –1.5 V/ SHE. This potential precisely corresponds to the oxidation potential of the excited state of the dye and therefore indicates that amorphous alumina could directly mediate electron transfer from the dye excited states to the conduction band of TiO_2 [73].

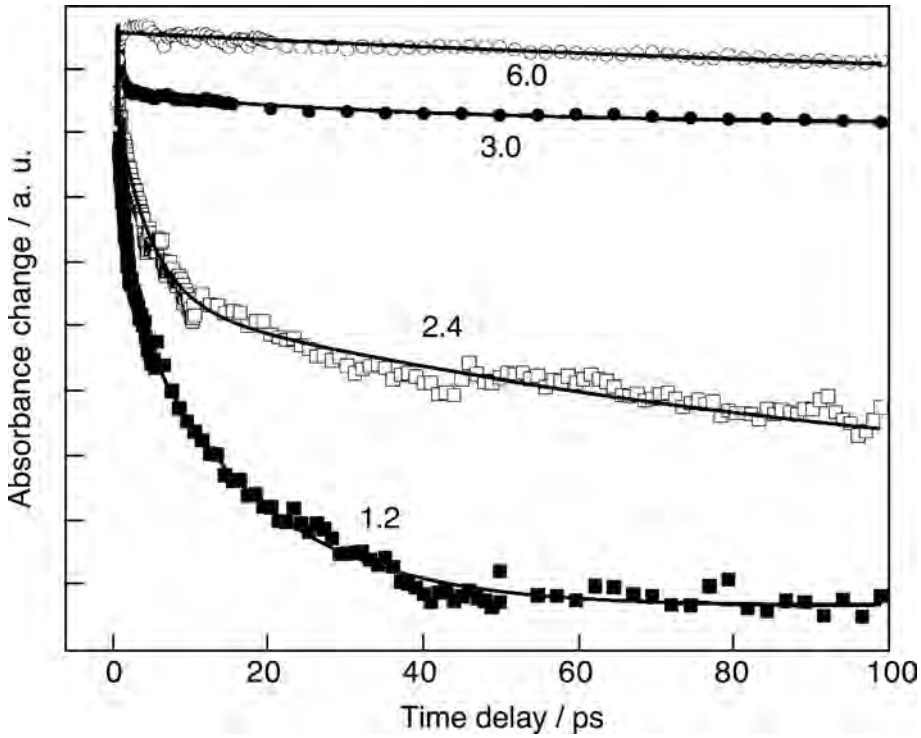

Figure 11.14 Transient absorption decay of the photoexcited state of Ru^{II}(4'-PO_3-tpy)$(NCS)_3$ dye adsorbed onto Al_2O_3/ TiO_2 core-shell nanocrystalline films measured by pump (λ = 530 nm) - probe (λ = 560 nm) fs laser spectroscopy. Alumina layer thickness was 1.2 nm, 2.4 nm, 3.0 nm, and 6.0 nm [73].

An interesting example of strong electronic coupling case is provided by the alizarin | TiO_2 system [32,77]. Chelation of surface Ti(IV) sites by alizarin (1,2-dihydroxy-anthraquinone) results in the red shift of the absorption spectrum of the dye by 70 nm due to deprotonation of both hydroxy groups. The question has been addressed whether the excited state orbital of adsorbed alizarin extends into the solid and involves the orbitals of the Ti^{4+} ion. Computational results suggest indeed a substantial electron density on surface Ti^{4+} in the HOMO and thus the formation of a ground-state charge transfer complex. In the LUMO, however, electron density shifts back to the π^* orbitals of the conjugated rings, indicating that the transition has no, or weak ligand-to-metal charge transfer character [78]. This conclusion was confirmed by resonance Raman and Stark effect spectroscopies [79], thus ruling out the possibility that charge injection into TiO_2 takes place through a resonant mechanism. Light excitation of alizarin | TiO_2 surface complexes results in an adiabatic electron injection process, which was observed to occur within only 6 fs [80]. Despite this apparently very strong electronic coupling, a sequential mechanism involving the prior formation of a localized molecular excited state, followed by sub-10 fs electron transfer was indeed observed by optical pump - probe transient absorbance spectroscopy [80].

11.3.2 Charge recombination

The rate of the electron recapture which takes place between the solid and the oxidized dye species S^+ (Eq. 11.4) has been observed to be generally slower by up to 10 orders of magnitude compared to charge injection rates of efficient sensitizers. Studies of TiO_2 colloidal dispersions and mesoporous nanocrystalline films sensitized by Ru(II)-polypyridyl complex dyes established that charge recombination indeed occurs on a tens- to hundreds of microseconds time scale. Four main reasons can be invoked to explain such a huge difference :

a) Contrary to the charge injection process, where the electron is transferred to a continuum of acceptor levels, back electron transfer takes place from the solid to a discrete electronic state of the oxidized dye molecule. As a consequence, the density of states FCWD (Eq. 11.14) in the successor system is orders of magnitude smaller than for the forward ET reaction.

b) While electron injection is generally activationless and thus kinetically optimal, the high exoergicity of the back transfer can make the system lie deep in the inverted Marcus region, where the rate of the charge transfer process is expected to decrease with increasing driving force.

(c) In efficient dye sensitizers, the LUMO extends over the molecule's moiety that is directly anchored to the surface of the oxide semiconductor, thus ensuring a strong donor-acceptor electronic coupling. The charge recombination process takes place from the solid to the HOMO of the dye, which is ideally localized as far as possible from the surface (Fig. 11.15). Hence, the electronic coupling matrix element $|H|$ for the electron recapture process is considerably reduced. The positive charge left in the HOMO of the sensitizer can delocalize even further apart from the surface on electro-donating ligands, such as –NCS, or donor moieties, like in redox heterotriads [81,82]. Lateral electron transfer across the surface constitutes an additional degree of freedom for the delocalization of positive charges. A self-exchange electron transfer reaction mechanism (charge hopping between co-adsorbed sesnsitizer molecules) allow positive charges to percolate within densely packed adsorbate layer away from the position where the electron was initially injected [83].

(d) Finally, and perhaps more importantly, conduction band electrons readily thermalize and get trapped in intraband states. The dynamics of trapping and detrapping and carriers transport within the solid particle network can control the overall reaction kinetics that would not then depend upon the sole interfacial electron transfer rate.

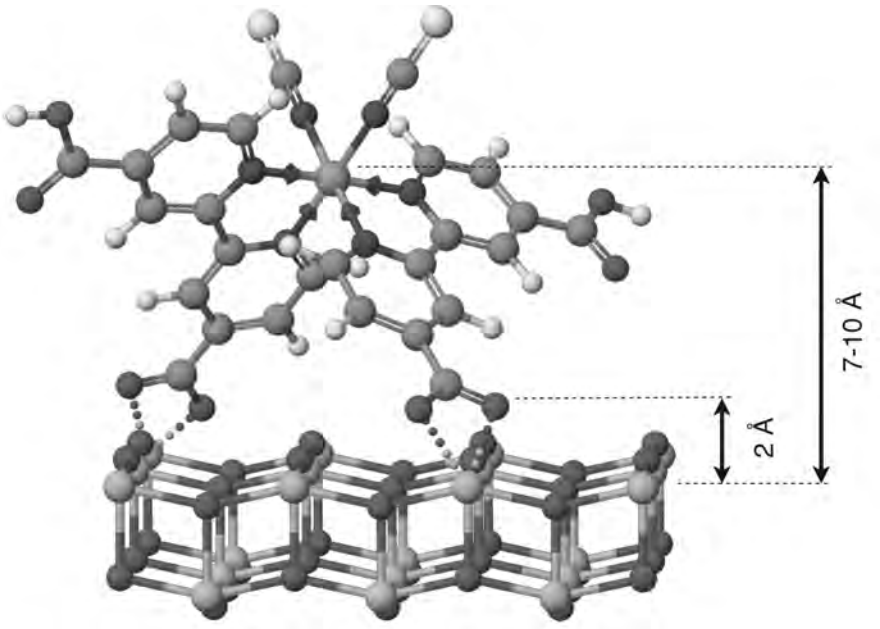

Figure 11.15 Ball-and-stick molecular model of $Ru^{II}(dcbpy)_2(NCS)_2$ dye adsorbed onto TiO_2 anatase. While charge injection takes place from the π^* LUMO extending over the carboxylic anchors directly bond to surface Ti^{4+} ions, back ET returns the electron to the d-orbital (HOMO) localized on the Ru(III) center, *ca* 7 Å apart from the surface.

Dependence of back electron transfer rate upon nuclear reorganization

Efficient dye sensitizers of oxide semiconductors are generally characterized by an oxidation potential of their excited state $\phi^o(S^+/S^*)$ that is close to the conduction band flatband potential of the solid. As a consequence, the free Gibbs energy $\Delta G_b^{\ 0}$ of the back electron transfer can be as negative as –1 to –2 eV, depending on the potential assumed for free and/or trapped electrons involved in the reaction. The total reorganization energy Λ associated with the heterogeneous charge transfer process is typically of the order of 0.5 eV, and is therefore smaller than the reaction driving force ($\Lambda < -\Delta G_b^o$). In terms of current electron transfer theory, this situation, depicted by Figure 11.16, corresponds to an inverted energetic / kinetic region.

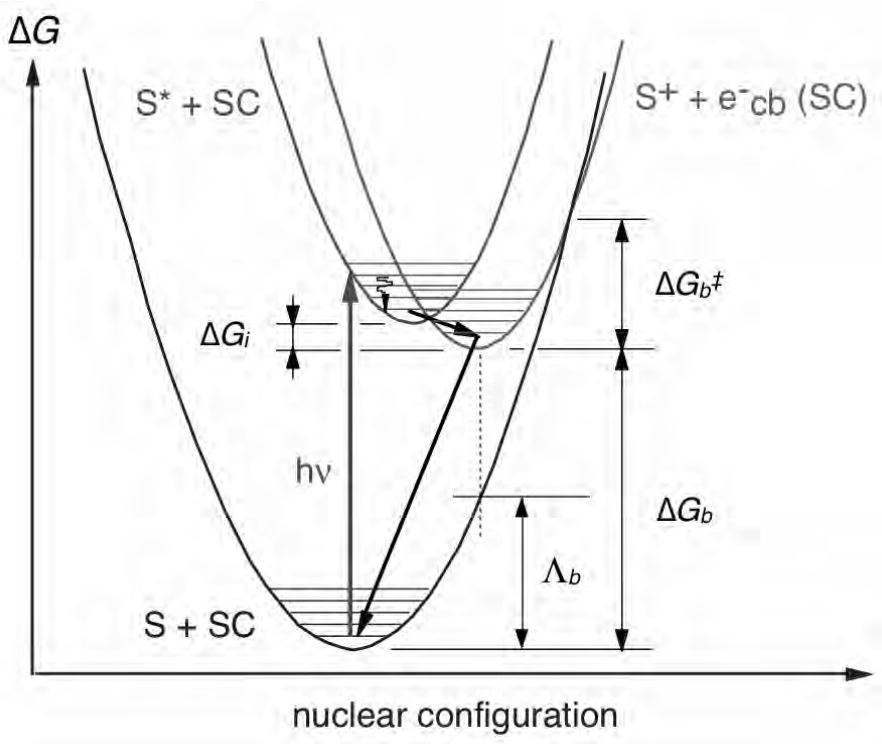

Figure 11.16 Potential energy parabolas of the three states involved in the interfacial electron injection and back transfer. While injection is essentially activationless, the recombination process lies in the inverted Marcus region with $-\Delta G_b > \Lambda_b$.

For a non-adiabatic process the rate constant is generally expressed by Fermi's golden rule (Eq. 11.14). Within the classical limit, where the frequency of the vibrational modes associated with the activated complex formation is small ($h\nu << kT$) , Marcus' classical quadratic relationship applies with :

$$FCWD = \sqrt{2\pi\ \Lambda\ k_B T}\ \exp\left(\frac{-\Delta G^{\ddagger}}{k_B T}\right) \tag{11.19}$$

$$\Delta G^{\ddagger} = \frac{\left(\Delta G^0 + \Lambda\right)^2}{4\Lambda} \tag{11.20}$$

where $\Delta G^{\ddagger}$ is the reaction activation and Λ the nuclear reorganization energy.

This classical expression is not generally adequate to describe the kinetics of ET within the inverted region. The potential energy surface of the precursor state $S^+ \mid SC(e_{cb}^-)$ in this case indeed appears inside the PES of the successor complex $S \mid SC$, allowing vibrational wavefunctions of both states to strongly overlap and making nuclear tunneling underneath the activation barrier particularly efficient. This effect is taken into account in a semi-classical description of the nuclear factor FCWD, where internal vibrations, approximated by a single collective high frequency vibrational mode ($h\nu > kT$), are treated quantum mechanically, while solvent reorganization and internal low frequency modes are grouped in a continuum of states and considered classically :

$$FCWD = \sqrt{2\pi\ \Lambda_s\ k_B T}\ \exp\left(\frac{-\Lambda_v}{h\nu}\right) \sum_{w=0}^{\infty} \frac{1}{w!} \left(\frac{\Lambda_v}{h\nu}\right)^w \exp\left(\frac{-\left(\Delta G^0 + wh\nu + \Lambda_s\right)^2}{4\Lambda_s\ k_B T}\right) \tag{11.21}$$

and for the rate constant :

$$k_{ET} = \sqrt{\frac{\pi}{h^2 \Lambda_s\ k_B T}}\ |H|^2 \exp\left(\frac{-\Lambda_v}{h\nu}\right) \sum_{w=0}^{\infty} \frac{1}{w!} \left(\frac{\Lambda_v}{h\nu}\right)^w \exp\left(\frac{-\left(\Delta G^0 + wh\nu + \Lambda_s\right)^2}{4\Lambda_s\ k_B T}\right) \tag{11.22}$$

where $|H|$ is the electronic coupling matrix element, Λ_v and Λ_s are the high frequency mode (inner sphere) and low frequency modes (inner- and outer-sphere) terms of the reorganization energy ($\Lambda = \Lambda_v + \Lambda_s$), respectively. Computation of Eq. 11.22 (Fig. 11.17) shows that the quantum treatment of high frequency vibrational modes has a marked effect in the inverted Marcus region. The large Franck-Condon coupling that characterizes generally the inverted region renders nuclear tunneling a dominant process. The first consequence of this effect is a drastic decrease of the dependence of

the electron transfer rate upon its energetics. Nuclear tunneling underneath the nuclear reorganization barrier also means the electron transfer process in these conditions becomes practically activationless. As a second consequence, it is therefore expected that the temperature dependence of the electron transfer kinetics disappears.

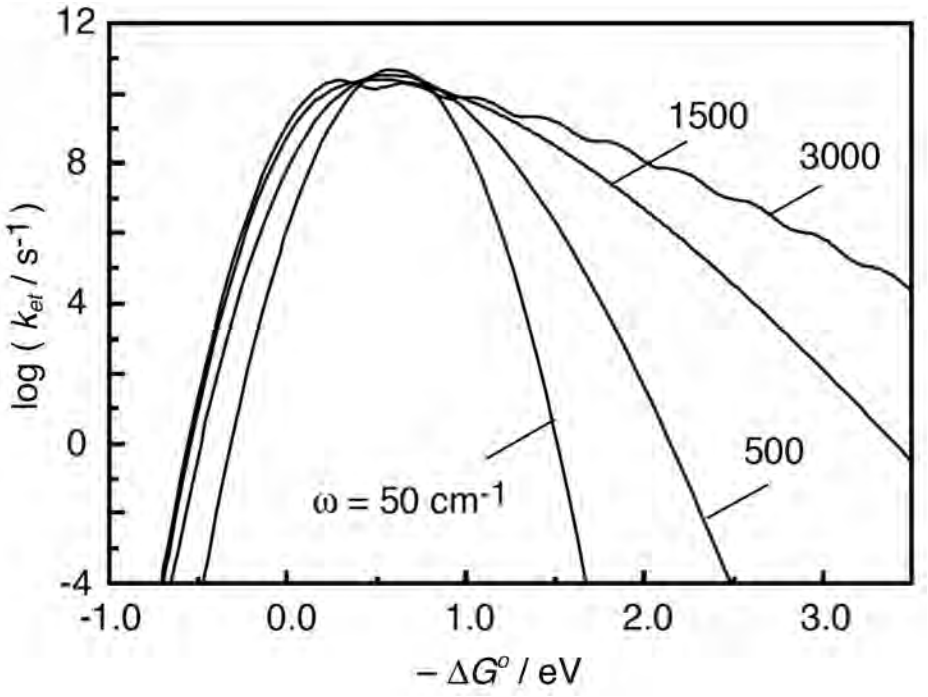

Figure 11.17 Computation of Eq. 11.22 with $|H| = 10$ cm^{-1}, $\Lambda_v = 0.3$ eV, $\Lambda_s = 0.2$ eV, and increasing values of the average high frequency mode wavenumber ω. Introduction of the quantum mechanics treatment of vibrational reorganization modifies markedly the prediction of the model compared to that of the classical theory ($\omega \leq 50$ cm^{-1}). The difference is much more important in the Marcus inverted region ($-\Delta G > \Lambda$), where Franck-Condon coupling is larger.

Numerous experimental evidences of inverted region behavior of the charge recombination reaction were reported [77,84,85]. The dynamics of the electron back transfer from the conduction band of TiO_2 nanoparticles to the cations of various organic sensitizers, such as alizarin, merocyanine and coumarin dyes, was investigated in

alcoholic colloidal dispersions. It was observed to be practically insensitive to temperature over a window of more than 200 K [77]. Although the highly exergonic recombination reaction was concluded to fall deeply in the Marcus kinetic inverted region, it is evident from the temperature independent rate constants that the recombination proceeds essentially as if it would not be controlled by activation.

In accordance with the predictions of the semi-classical model of Eq. 11.22, observations of a pseudo-activationless behavior [77,86] show that the inverted kinetic region situation of the back electron transfer process cannot be generally invoked as the cause of its slow kinetics. Light intensity and applied potential bias dependence studies tend to demonstrate that the back-ET kinetics is primarily controlled by the distribution and occupancy of trap states in the band gap of the semiconductor and electron transport in the solid particle network [30,31,86-90].

Experimental determination of the back electron transfer rate

Transparent mesoposous, nanocrystalline TiO_2 films allow the back electron transfer process to be observed in real time using transmittance mode spectroscopy in conjunction with ns pulsed laser excitation. Dynamic and mechanistic insights have been gained from transient absorption measurements made under open-circuit conditions in the absence of an external electron donor, such as each injected electron recombines with an oxidized sensitizer species. Typical experimental setups based on high repetition rate laser sources can currently achieve time-resolved measurements of transient absorbance changes $\Delta A < 10^{-4}$. In the case of *cis*-$[Ru^{II}(dcbpy)_2(NCS)_2]$-sensitized TiO_2, the kinetics of the recombination reaction (Eq. 11.4) can be followed by observing in real time the decay of the absorption of the dye cation S^+ at $\lambda_{obs} > 630$ nm, or the recovery of the dye ground-state absorption at $\lambda_{obs} < 600$ nm (Fig. 11.10).

A common source of discrepancy between reported recombination kinetics measured for identical systems is due to different laser pulse intensities used to excite the dye. In mesoporous films, if diffusion of injected electrons from one nanoparticle to the neighboring ones is slow compared to the recombination reaction, e_{cb}^- / S^+ pairs produced during the charge injection process (Eq. 11.2) are confined to the restricted volume represented by one single oxide particle. The recombination kinetics obviously depends on the average number $< x >$ of reactive pairs per particle and, thus, upon the excitation light intensity. This situation is comparable to that of e^-/ h^+ recombination in semiconductor particles under bandgap irradiation [91]. While a first order kinetics should prevail for $< x > \leq 1$, a faster dynamics is expected for larger $< x >$ values, eventually reaching a second order kinetic regime when $< x > \geq 20$ [91].

The average number $< x >$ of e_{cb}^- / S^+ pairs produced per illuminated spherical particle in a dye-sensitized nanocrystalline film can be estimated from the values of the excitation wavelength λ_{ex}, the energy fluence per laser pulse F_{ex}, the absorbance A of the dye at λ_{ex}, the average particle radius r, the thickness of the mesoporous film d, and its porosity φ :

$$< x > = \frac{\lambda_{ex} \cdot F_{ex} \cdot \left(1 - 10^{-A}\right) \cdot 4\pi \cdot r^3}{3\ h \cdot c \cdot d \cdot \varphi} \qquad (11.23)$$

Assuming for a typical sample submitted to a flash photolysis experiment : $\lambda_{ex} = 600$ nm, $A = 1.5$, $r = 10$ nm, $d = 8$ µm, and $\varphi = 0.5$, the condition that $< x > \leq 1$ implies the excitation energy fluence of the laser is $F_{ex} < 33\ \mu J \cdot cm^{-2}$. This energy density is quite low compared to typical laser intensities used for time-resolved experiments and requires normally the excitation laser pulse is strongly attenuated through neutral density filters or expanded by a diverging lens before reaching the sample. In ultrafast laser spectroscopy experiments, pump and probe laser beams are

usually focused on a very small spot on the sample, which dimensions are of the order of a few tens of microns. As a consequence, experimental conditions typically used to monitor the charge injection dynamics result in the excitation of a majority of the dye molecules and in the production of a large number of e_{cb}^{-} / S^{+} per particle, often with $< x >$ values approaching 100. Recombination kinetics observed in these cases are usually very fast and impossible to compare with data collected using ns flash photolysis setups and controlled attenuated excitation energy.

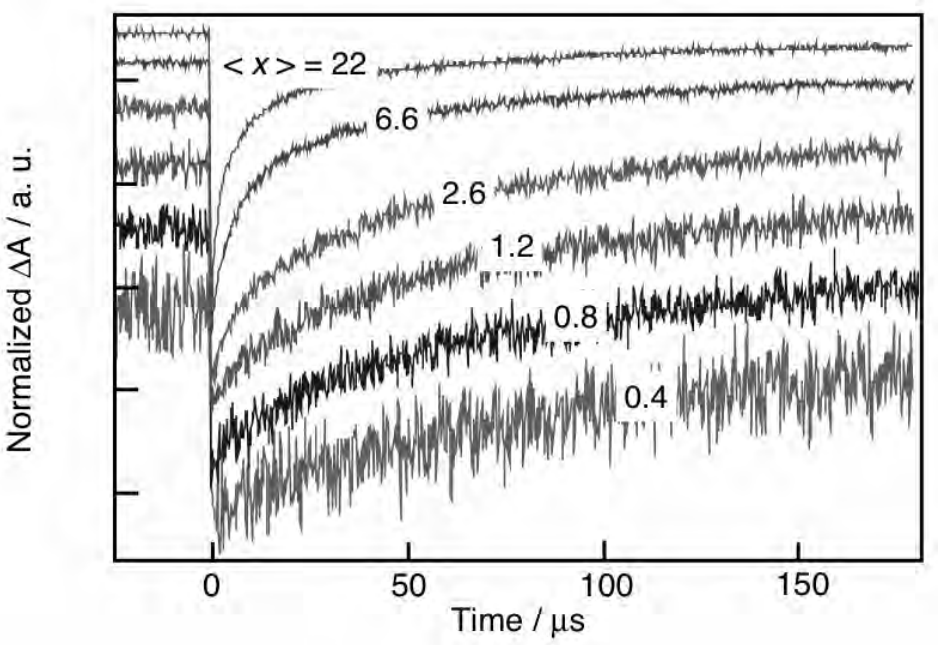

Figure 11.18 Temporal evolution of the transient absorbance changes measured upon laser excitation of N-719 dye adsorbed on mesoporous TiO_2 films in MPN solvent. Bleaching signals observed at $\lambda = 520$ nm appear within the ns laser pulse as the result of ultrafast charge injection. Recovery of the initial absorption of the dye ground state follows the back electron transfer kinetics. The intensity of the excitation laser pulse ($\lambda = 600$ nm) was varied as to inject an increasing number of electrons per pulse into the solid. The calculated average number $< x >$ of e_{cb}^{-} / S^{+} pairs produced per nanoparticle is indicated on the respective traces.

Figure 11.18 displays the kinetics observed for the back electron transfer reaction following charge injection from photo-excited N-719 dye into mesoporous TiO_2 films. At low excitation light intensity, yielding $< x > = 0.4$, a half reaction time $t_{1/2} = 100$ µs is estimated from the trace, which could be fitted by a first order rate law with $k_b = 7 \cdot 10^3$ s^{-1}. Increasing the laser pulse intensity results in faster recombination kinetics that can hardly be fitted by an exponential law anymore. $t_{1/2}$ is observed to be shortened to ~ 50 µs for $< x > = 1.2$, and further to 20 µs, 10 µs, and 3 µs at $< x > = 2.6$, 6.6 and 22, respectively.

Large optical densities of dyed samples of the order of $A = 1$-2 imply that light is attenuated considerably through the film. The intensity reaching the first layer of particles at the illuminated surface is therefore approximately one or two orders of magnitude larger than that attaining the bottom layer. This effect is likely to cause a large spread of the number of e_{cb}^- / S^+ pairs produced per nanoparticle and inhomogeneity in the kinetics observed globally by transient transmittance spectroscopy. In practice, with dye sensitized films exhibiting typically an absorbance $A = 1.5$ at the laser excitation wavelength, the observed recombination kinetics keeps on changing upon decreasing excitation intensity, until the laser fluence is dimmed below 12 µJ · cm^{-2} ($< x > \approx 0.4$).

Distance dependence of back electron transfer dynamics

Reaction rate due to distance-dependent electron tunneling from conduction band electrons $TiO_2(e_{cb}^-)$ to surface bound oxidized dye S^+ acceptor species should follow an exponential dependence upon spatial separation, as observed for the electron injection process. Using sensitizers anchored to the surface of titanium dioxide through bridges of various length and redox heterotriad structures, several studies reported indeed rate constants following Eq. 11.18 with a damping factor of the order of $\beta = 1.0$ Å^{-1},

corresponding to through-space electron tunneling [2,81,82,92]. Spectacular extension of the lifetime of light-induced charge-separated states to over several seconds was reported in particular for heterotriads made of ruthenium complexes anchored to nanocrystalline TiO_2 and covalently linked to a polymeric chain of triphenylamine groups. The half-time for the recombination process between the injected electron and the oxidized amine increased from 350 ms to 5 ms and to 4 s as the number of triphenylamine subunits increased from 1 to 2 to 100, respectively [92].

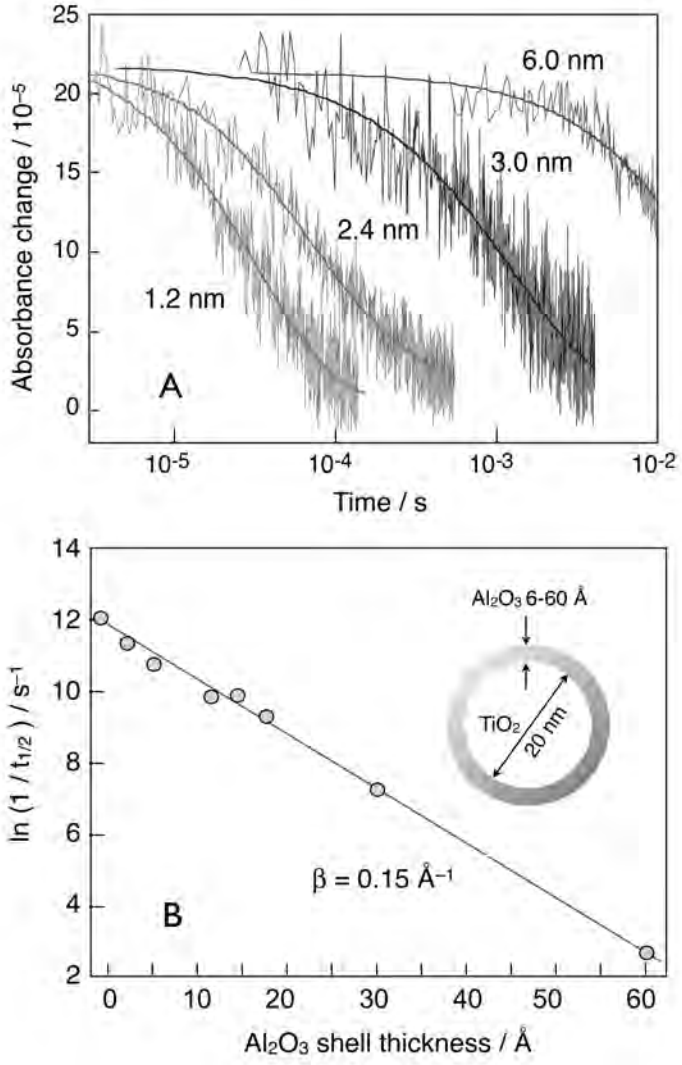

Figure 11.19 (A) Transient absorption decay of the oxidized state of Ru^{II}(4'-PO_3-tpy)$(NCS)_3$ dye adsorbed onto Al_2O_3/ TiO_2 core-shell nanocrystalline films. Alumina

layer thickness was 1.2 nm, 2.4 nm, 3.0 nm, and 6.0 nm. λ(pump) = 535 nm, λ(probe) = 650 nm. Laser pulse fluence $F_{ex} = 20$ μJ/ cm^2. (B) Dependence of the observed back electron transfer time constant 1/ $t_{1/2}$ upon the thickness of the coating layer [2,73].

Phosphonated ruthenium terpyridyl complex $Ru^{II}(4'\text{-}PO_3\text{-tpy})(NCS)_3$ adsorbed on transparent mesoporous films made of core/ shell TiO_2 particles coated by layers of Al_2O_3 of increasing thickness was mentioned above (Fig. 11.14) for electron injection. The same system can be used to study the distance dependence of the charge recombination kinetics without having to change the actual molecular structure of the dye sensitizer [73]. Figure 11.19 shows that tunneling of e_{cb}^- (TiO_2) through the alumina layer to dye cations adsorbed on the outer surface is considerably increasing the half lifetime of the charge separated state from 6 μs on naked TiO_2 to 60 ms for a 6 nm-thick alumina overlayer (Fig. 11.19). Analysis of the donor-acceptor spatial separation dependence yields a damping factor $\beta = 0.15$ Å^{-1}. Compared to the values of $\beta = 0.04$ - 0.11 Å^{-1} obtained for the electron injection process, this latter figure indicates that recombination rate is apparently attenuated in a greater extend than forward ET. This particular behavior of an unusual weak distance dependence of charge injection was also observed for *p*-oligophenylene-bridged sensitizers adsorbed on TiO_2 [73,74]. In this case, this effect is believed to be due to the coupling of the tunneling electrons to non-equilibrium longitudinal vibrational modes of the phenylene molecular bridge [74]. As the same rationale is hardly applicable to the alumina spacer case, this effect will certainly deserve more attention.

Role of trap states in non-exponential recombination kinetics

Under experimental conditions where the injected electron always returns to the same dye molecule, because of geminate recombination or because the injected electron and the dye cation are confined within a single solid particle, back electron transfer reaction should follow a first order kinetics. Unlike colloidal dispersions, for which back-electron transfer process has been found to generally follow a single exponential

rate law [93], charge recombination observed on dye-sensitized mesoporous TiO_2 films usually display intricate non-exponential kinetics. Temporal evolution of the recombination reaction is generally well described by the Kohlrausch-Williams-Watts (KWW) stretched exponential function (Eq. 11.24), where $C(t)$ is the concentration of the reacting dye cation at time t, C_o the initial concentration, k_o a representative modal first order rate constant, and $0 < \gamma \leq 1$ a dispersion parameter inversely related to the width of the rate constant distribution.

$$C(t) = C_o \cdot \exp\left[\left(- k_o \cdot t\right)^{\gamma}\right] \tag{11.24}$$

Fitted parameters k_o and γ, however, do not provide much physical insights and the dynamics is preferably characterized by the half-reaction time $t_{1/2}$ and an average first-order rate constant $<k> = 1/ t_{1/2}$. This peculiarity of sintered membranes could be rationalized in terms of trapping of injected electrons at grain-boundaries and at sites that are absent in dispersed colloidal particles, where the reaction in the presence of surface-complexing dyes is believed to involve free conduction-band electrons or carriers that are localized in shallow traps [3]. Interestingly, as the back electron transfer process becomes sufficiently slow, for instance by increasing the reaction distance with a wide spacer, the dispersion of Eq. 11.24 is generally observed to become narrower ($\gamma \rightarrow 1$) and the kinetics eventually to follow a simple first order rate law with $k_b = k_o = (1/ t_{1/2}) \cdot \ln 2$ [92,94].

Multiexponential kinetics of back electron transfer processes were reported in numerous recent publications. Although it was suggested the complex kinetics could be due to vibrational relaxation and solvation of the dye oxidized state produced initially by the back electron transfer reaction [95], the role of trapping sites in nanocrystalline porous semiconducting electrodes was clearly identified by examining the bias potential dependence of the recombination rate [29,31,96]. The rate of recombination of injected

electrons with oxidized sensitizer molecules is strongly dependent upon the concentration of electrons imposed by the applied potential in the conduction band and trap states. Haque et al. scrutinized the parameters influencing charge recombination kinetics in N-719 dye-sensitized nanocrystalline TiO_2 films and found it was strongly dependent upon excitation intensity, electrolyte composition, and the application of an electrical bias to the semiconductor oxide [31].

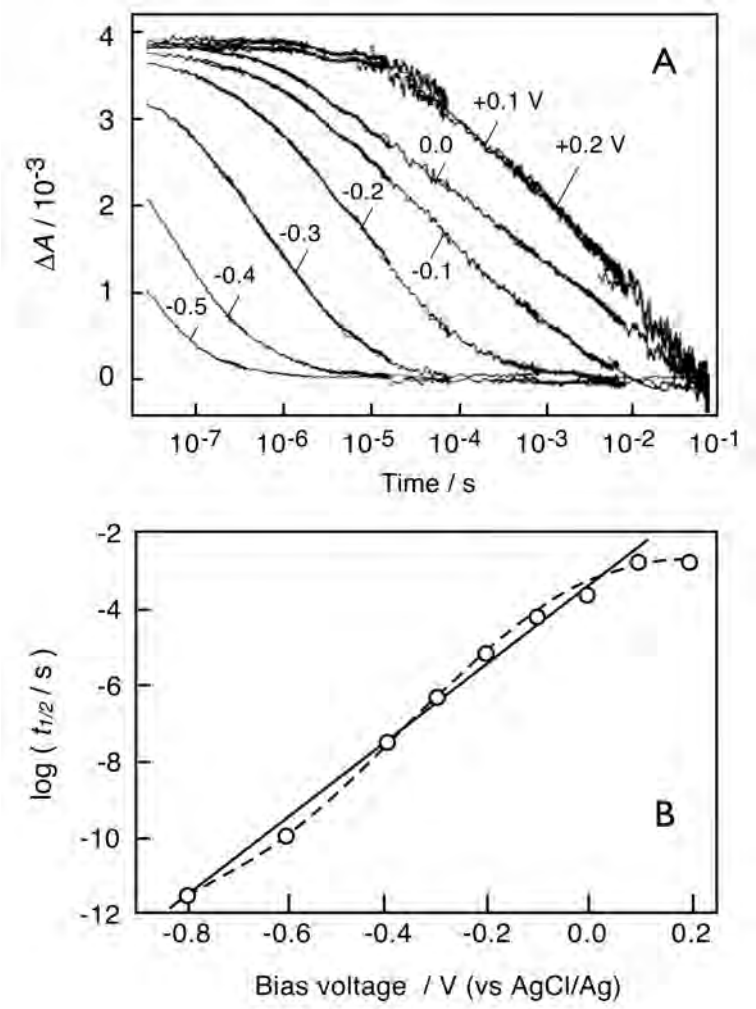

Figure 11.20 (A) Transient absorption decay of the oxidized state of N-719 dye-sensitizer adsorbed on a TiO_2 nanocrystalline electrode under potentiostatic control. Dependence of the charge recombination kinetics upon the applied potential is shown for potentials ranging from + 0.2 V to – 0.5 V vs AgCl/ Ag. (B) Dependence of the

back-electron transfer kinetics upon applied potential for a N-719-sensitized nanocrystalline TiO_2 electrode. Experimental conditions and data are those of Haque et al. [31].

Figure 11.20 (A) displays absorption transients collected for potentials applied to a mesoporous TiO_2 electrode sensitized by N-719 dye ranging from + 0.2 V to – 0.5 V vs AgCl/ Ag. These data exhibit non-single-exponential behavior. While at applied potentials of + 0.1 V and + 0.2 V charge recombination follows similar kinetics, reduction of the bias voltage below 0 V increases the reaction rate by several orders of magnitude [30]. A plot of log ($t_{1/2}$) versus the applied potential, Fig. 11.20 (B), shows a ten fold augmentation of the rate for every 100 mV increase in the forward bias potential. A simple comparison with data reported in Fig. 11.18, where a half-reaction time $t_{1/2}$ = 100 μs was obtained in open circuit conditions, indicate that in the absence of electrical and light bias the potential of the TiO_2 film is roughly equal to 0 V vs AgCl/ Ag reference electrode.

At a constant applied potential, the charge recombination kinetics were found to be also dependent upon electrolyte composition [31]. This strong dependence correlated with the shift of the energetic position of the conduction band/ trap density of states which is affected by the nature of the solvent and the presence of potential determining ions. Similarly to the bias voltage dependence, a 500 mV negative shift of the conduction band edge of TiO_2 induced by a variation in the electrolyte composition caused an acceleration in the recombination rate by more than five orders of magnitude. These observations show that the kinetics of charge recombination between electrons injected into nanocrystalline oxide films and adsorbed dye cations are strongly dependent upon the occupancy and energetics of the electronic states of the solid .

A numerical model based on the continuous-time random walk theory (CTRW) was applied to explain the stretched exponential kinetics and strong potential bias dependence of the recombination reaction. Observed kinetics was well described by

such a model and a KWW function, thus indicating that the back electron transfer process is controlled by dispersive electron transport between energetically and spatially distributed trap sites within the oxide nanoparticles [87,89,97,98].

11.4 ELECTRON TRANSFER DYNAMICS INVOLVING THE REDOX MEDIATOR

Conditions prevailing in operating DSCs at the maximum power extraction point correspond to a potential of the titanium dioxide photoanode approximately 500 mV more negative than the electrochemical potential of the mediator. The standard electrochemical potential of the triiodide/ iodide redox couple in aprotic solvents, such as propylene carbonate and acetonitrile, is roughly $\phi^0 (I_3^-/ I^-) = + 0.21$ V *vs* AgCl/ Ag [99]. For an iodide-based electrolyte, with typically 10 % added iodine, the Nernst potential of (I_3^-/ I^-) couple would then establish approximately at + 0.15 V and the corresponding Fermi potential in the TiO_2 at $\phi_F \cong - 0.35$ V *vs* AgCl/ Ag. In the case of the N-719 | TiO_2 system, recombination between conduction band electrons and oxidized dye sensitizer species at the interface (Eq. 11.4) would in such operating conditions take place within less than 1 μs (Fig. 11.20).

Interception of the dye cation must be sufficiently fast as to compete successfully with the unwanted charge recombination. According to Eq. 11.7, and approximating the kinetics of the back-electron transfer (Eq. 11.4) by an exponential law with $k_b = 10^6$ s^{-1}, a pseudo first-order rate constant $k_r \geq 10^7$ s^{-1} for the reduction of the dye oxidized state by the mediator (Eq. 11.5) would be required to ensure that the dye regeneration yield is at least 90 %. This stringent requirement is relatively difficult to meet with practical electrolytes. The dynamics of the interception of the dye cation by the mediator is therefore key to the overall performance of DSCs.

The operating voltage of the solar cell (~ 0.5 V) corresponds also to the driving force of the indirect recombination process, taking place between conduction band electrons in the semiconductor and the oxidized mediator (Eq. 11.6). The latter interfacial reaction is at the origin of the dark current observed in DSCs and its occurrence involves both a decrease of the photocurrent and of the open-circuit voltage

of the photovoltaic device. Transport of positive charges through the mediator (liquid or solid) to the counter electrode is therefore equally crucial for the energy conversion efficiency.

11.4.1 Kinetics of interception of dye cations by a redox mediator

Dynamics of reaction involving iodide-based electrolytes

Iodide-based electrolytes have been found to be particularly suited for dye-sensitized photo-electrochemical solar cells based on nanocrystalline TiO_2, ZnO or SnO_2. I^- anions are able to rapidly regenerate the sensitizer, while the indirect recombination process between e_{cb}^- (TiO_2) and I_3^- appears to be particularly slow. In these devices no other known redox couple works nearly as well. In solution iodide is capable of quenching reductively the excited state of many molecular dyes. On a semiconductor surface, such as SnO_2 and TiO_2, however, reductive quenching of non-aggregated sensitizer molecules by iodide is not able to compete kinetically with the ultrafast charge injection [2,100].

The detailed mechanism of the two-electron transfer dye regeneration reaction (Eq. 11.5) has not been fully elucidated and many factors appear to influence its rate. The following one-electron transfer reactions can in principle take place on the surface of the oxide and account globally for the oxidation of iodide to triiodide [2,101] :

$$S^+ | TiO_2 + I^- \rightarrow S | TiO_2 + I^{\cdot} \quad (11.25)$$

$$I^{\cdot} + I^- \rightarrow I_2^{-\cdot} \quad (11.26)$$

$$S^+ | TiO_2 + 2\,I^- \rightarrow S | TiO_2 + I_2^{-\cdot} \quad (11.27)$$

$$2\,I_2^{-\cdot} \rightarrow I^- + I_3^- \quad (11.28)$$

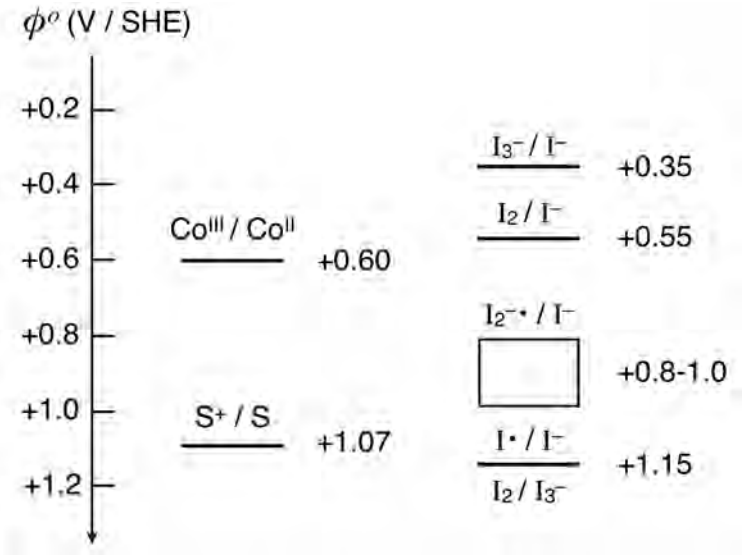

Figure 11.21 Diagram of standard potentials *vs* SHE (aq.) for redox couples relevant to the dye regeneration in acetonitrile. ϕ^0 (S^+/S) is indicated for N-3 dye [33]. Potentials of (I_3^-/ I^-), (I_2/ I^-) and (I_2/ I_3^-) couples were taken from ref. [99]. ϕ^0 ($I^\bullet$/I^-) in acetonitrile is extracted from [102]. In aqueous solution, potentials of ($I^\bullet$/I^-) and ($I_2^{-\bullet}$/I^-) couples are +1.33 V and +1.03 V/ NHE, respectively [2]. In acetonitrile ϕ^0 ($I_2^{-\bullet}$/I^-) should be lower than in water, with a value of *ca* +0.9 V. ϕ^0 (Co^{III}/ Co^{II}) indicates the standard one-electron oxidation potential of the $Co^{II}(dbbip)_2^{2+}$ complex [103,104].

Figure 11.21 displays a diagram for the redox chemistry of iodide. Oxidation of I^- to $I_2^{-\bullet}$ radical is thermodynamically more favorable than the reaction leading to the iodine atom. Thus, reaction of Eq. 11.27 is favored over that of Eq. 11.25, provided that (I^-, I^-) or (S^+, I^-) ion pairs are present in significant amounts [101].

Dynamics of electron transfer between oxidized ruthenium(II) polypyridyl complexes and halide ions in heterogeneous systems has been probed employing experimental conditions and methods similar to those used to monitor the back electron transfer reaction in the absence of a redox-active electrolyte. Electrostatic binding of oxidized halide ions and ion pair formation on the surface of oxide semiconductor particles was proposed by several studies. The kinetics of re-reduction of the oxidized state of N-719 sensitizer adsorbed on nanocrystalline TiO_2 films by iodide was

measured by transient laser spectroscopy in the presence of various redox-inactive metal cations, whose role was to modulate the sensitized TiO_2 surface charge upon specific adsorption onto the oxide [13].

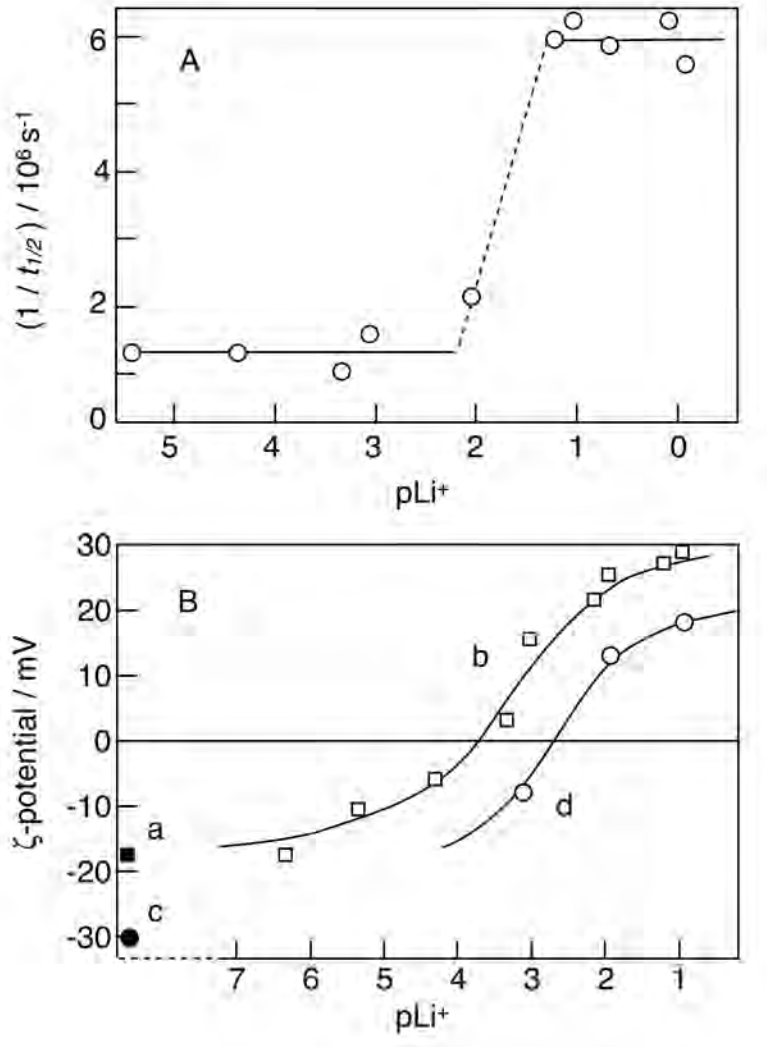

Figure 11.22 (A) Reciprocal half-reaction time ($1/t_{1/2}$) of N-719 dye regeneration following electron injection into TiO_2. Concentration of iodide $[I^-] = 0.1$ M in anhydrous propylene carbonate was kept constant, while $[Li^+]$ was varied. (B) Zeta-potential of undyed (b, □) and N-719-dyed (d, ○) titanium dioxide nanoparticles dispersed in dry propylene carbonate, determined by electrophoresis as a function of Li^+ concentration. Points labelled 'a' (■) and 'c' (●) represent ζ-potentials of naked and dye-sensitized particles, respectively, in PC solutions containing no Li^+ [13].

The rate of the reaction leading to the regeneration of the dye ground-state was found to depend strongly on the nature and concentration of cations present in the solution (Fig. 11.22) [13]. Small cations able to specifically adsorb onto the oxide surface, such as Li^+ and Mg^{2+}, favor the fast oxidation of iodide by the sensitizer's oxidized state. A sudden acceleration of the electron transfer process was observed at a critical cation concentration. Electrophoretic measurements showed that this concentration corresponds to the reversal of the titanium dioxide particle surface charge from negative to positive upon adsorption of ζ-potential-determining species. This observation was interpreted in terms of the switching from a reaction mechanism to another one, characterized by a different rate constant. The slower reaction path, that does not require the iodide anions to be adsorbed onto the surface, was attributed to the thermodynamically unfavorable oxidation of I^- to iodine atom (Eq. 11.25). Alternatively, the encounter of an intermediate complex (S^+, I^-) formed kinetically fast (Eq. 11.29) with a second iodide anion could yield $I_2^{-\bullet}$ radicals directly as a product of the electron transfer process (Eq. 11.30).

$$S^+ + I^- \rightleftarrows (S^+, I^-) \tag{11.29}$$

$$(S^+, I^-) + I^- \rightarrow S + I_2^{-\bullet} \tag{11.30}$$

$$S^+ + (I^-, I^-) \mid TiO_2 \rightarrow S + I_2^{-\bullet} \tag{11.31}$$

These reactions should be prevalent as long as the solid surface is negatively charged. When the surface zeta-potential is reversed to positive upon adsorption of small cations, a faster mechanism becomes predominant. Because it requires high local concentration of I^- on the surface of TiO_2, the latter was suggested to be due to the thermodynamically more favorable oxidation of I^- to $I_2^{-\bullet}$ that involves prior formation of (I^-, I^-) ion pairs on the surface (Eq. 11.31). Both mechanisms depicted by Eqs. 11.30 and 11.31 are based

on a fast pre-equilibrium and should thus be characterized by a second order kinetic law.

Durrant et al. reported a transient absorption study of the kinetics of re-reduction of ruthenium bipyridyl dye cations adsorbed to nanocrystalline TiO_2 films by iodide ions, employing a series of $Ru^{II}(dcbpy)_2X$ dyes, where (dcbpy) = 4,4′-dicarboxy-2,2′-bipyridyl and X = $(NCS)_2$, $(CN)_2$, Cl_2, and diethyl-dithiocarbamate (DTC) [105]. Data indicated that the regeneration reaction proceeded via a transient intermediate complex (S^+- I^-) formed by reaction of photogenerated dye cations with one iodide anion. The subsequent reaction of this complex with a second iodide ion, forming $I_2^{-\bullet}$, was shown to be the kinetically and thermodynamically limiting step in the overall regeneration reaction. A recent computational study of the interactions between I^- and N-719 dye sensitizer explored the various pathways that could lead to (S^+- I^-) adducts [106]. This work reached in particular the conclusion that a charge transfer adduct is likely to be formed between iodide and the sulfur atom of the thiocyanate ligand of the oxidized dye with a distinctive S – I bonding. Other plausible intermediate were analyzed based on an inner-sphere interaction between the ruthenium center and the redox mediator. In addition, computational evidence of a charge transfer process taking place between I^- and an intermediate $[Ru^{III}(dcbpy)_2(NCS)I]^+$ resulting from an initial ligand exchange reaction was identified.

In $Ru^{II}(dcbpy)_2X$–type dyes, some of the properties of the MLCT excited state are common to the oxidized species. As indicated by comparable absorption spectra, both species are characterized by similar electron densities on the Ru(III) center and the halide or pseudo-halide X ligands. As a result, intermediate charge transfer complexes are also likely to be formed between the electron-rich I^- anion and the electron-deficient Ru^{III} or X ligands in the dye excited state. Experimental evidence of such a complex formation was brought for $Ru^{II}(dcbpy)_3^{2+}$ dye adsorbed on the surface of aqueous TiO_2 colloidal particles [107]. A transient was observed in the λ = 700-800 nm spectral region

with an extinction coefficient 6 times larger than that of $I_2^{-\bullet}$, which was assigned to an adduct species (S*- I^-). Although similar in nature, the oxidation of I^- by S^+ and S* species of N-719 dye sensitizer on the surface of TiO_2 differ strongly on the kinetic point of view. While the interception of the dye cation by iodide takes place within approximately 100 ns in pure iodide ionic liquids ($[I^-] = 5.5$ M), reductive quenching of the excited state of ill-adsorbed N-719 dye molecules in identical conditions proceeds approximately 4 orders of magnitude faster, in the picosecond time scale.

While cooperative interaction of Ru(II) complex-based dyes with iodide has been observed in several systems, bulky ligands carried by the sensitizer molecules can also constitute a steric barrier for the approach of iodide species and affect negatively the regeneration process dynamics. Such an effect is particularly evident with Ru^{II}(4,4'-dcbpy)(4,4'-dinonyl-bpy)$(NCS)_2$ (Z-907) dye. The advantage of using an amphiphilic polypyridyl ruthenium sensitizer such as Z-907 for maintaining the DSC device stability was demonstrated [108]. Subsequently, Z-907 has been widely used with non-volatile, lithium-free 3-methoxy-propionitrile (MPN)-based electrolytes. A typical comparison between the kinetics of the interception of both N-719 and Z-907 dye cations by iodide is provided by Figure 11.23. In the presence of a concentration of iodide of $[I^-] = 0.7$ M in MPN, the regeneration of N-719 is characterized by a half-reaction time $t_{1/2} = 200$ ns. In identical conditions, this reaction is observed to be slower by approximately 2 orders of magnitude in the case of Z-907 sensitizer, for which a half reaction time $t_{1/2} = 15$ μs is observed. Such a drastic effect is attributed to the two nonyl groups equipping one of the Z-907 ligands.

These alkyl chains, whose role is precisely to constitute a hydrophobic barrier against possible adsorption of water onto the surface of TiO_2 and consequently adverse desorption of the dye, clearly impair the access of iodide anions to the Ru(III) center of the oxidized sensitizer species and/ or to te –NCS ligands. Although largely redundant in the case of N-719, the kinetics of the regeneration process for Z-907 is tightly

sufficient to compete with back electron transfer. Data of Fig. 11.24 show indeed that 20 µs after the laser pulse, 20 % of oxidized dye species would have undergone recombination with conduction band electrons in the absence of iodide. Over the same time period, approximately 30 % of Z-907 dye cations are remaining unreacted, while the regeneration of N-719 dye is complete. Application of Eq. 11.7 with $k_r = 1/t_{1/2} = 6.7 \cdot 10^6\ s^{-1}$ and $k_b = 5.6 \cdot 10^4\ s^{-1}$ leads to a competition yield $\eta_r = 92\ \%$, indicating that 8 % of the separated charges would have recombined in these conditions.

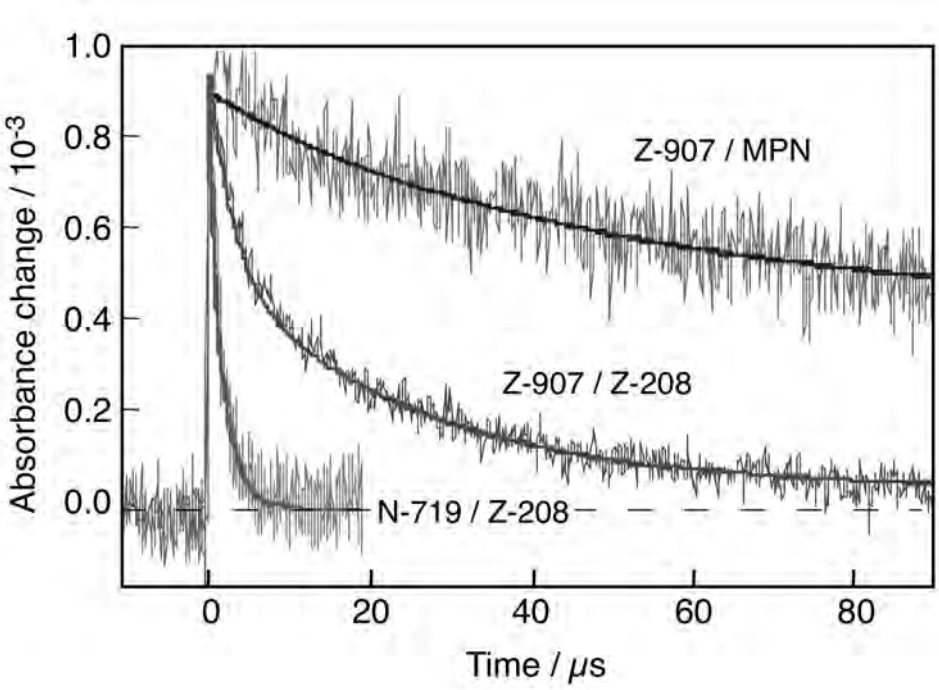

Figure 11.23 Transient absorption decay kinetics of the oxidized state of N-719 and Z-907 dyes adsorbed on nanocrystalline TiO_2 films in pure MPN solvent and in a non-volatile, lithium-free electrolyte, coded Z-908, containing $[I^-] = 0.7$ M in MPN. Half reaction times measured for the systems Z-907/ MPN, Z-907/ Z-908, and N-719/ Z-208 are $t_{1/2} = 180$ µs, 15 µs, and 200 ns, respectively.

Slow intrinsic oxidation of iodide by the oxidized sensitizer cations must be compensated by the use of large concentrations of iodide. Due to the limited solubility of conventional iodide salts, such as LiI and TBAI, addition of ionic liquids has been found to provide a simple way to obtain practically interesting iodide concentrations of the order of 1-2 $mol \cdot l^{-1}$ in MPN solvent. Figure 11.24 (a) shows the iodide concentration dependence of the reciprocal half-reaction time $k_r' = 1/t_{1/2}$ for the regeneration of Z-907 dye [51]. Addition of increasing amounts of PMII (N-propyl-N'-methyl-imidazolium iodide) ionic liquid in MPN allowed to obtain iodide concentrations up to $[I^-] = 2.5$ M. The obtained dependence is not linear for $0 < [I^-] < 1.5$ M, showing that the kinetics cannot be simply approximated by a pseudo first-order rate law at lower concentrations. The slope of the function $1/t_{1/2} = f([I^-])$ increases from a value of $2 \cdot 10^4\ M^{-1} \cdot s^{-1}$ for $[I^-] \leq 0.5$ M to $10^5\ M^{-1} \cdot s^{-1}$ for $[I^-] \geq 2$ M. As the iodide concentration exceeds 1.5 M, the slope remains invariable, yielding a second-order rate constant $k_r'' = 1 \cdot 10^5\ M^{-1} \cdot s^{-1}$. The observed sublinear function for $[I^-] < 1.5$ M in Fig. 11.24 (a) indicates that the apparent concentration of iodide reacting with S^+ species is smaller than the bulk concentration of the electrolyte. This suggests that a repulsive interaction exists between I^- anions and the dyed surface. A much higher value $k_r'' = 2 \cdot 10^7\ M^{-1} \cdot s^{-1}$ of the second order rate constant was observed for systems associating LiI electrolytes and N-719 dye-sensitizer, whose ligands do not carry any aliphatic chain and where the TiO_2 surface is expected to be positively charged [13].

Data sets (b) and (c) of Fig. 11.24 illustrate a case where attractive interactions are clearly prevailing between the dyed surface and the iodide mediator [109]. Dependence of the regeneration reaction kinetics upon the I^- concentration in the bulk of the electrolyte was studied in the case of an analog of Z-907 dye: $[Ru^{II}$(4,4'-dicarboxy-2,2'-bpy)(4,4'-dimethyl-2,2'-bpy)$(NCS)_2$ dye, coded N-820, that carries only methyl groups on one of its ligand, rather than nonyl aliphatic chains. The surface of

TiO_2 is found to be negatively charged after adsorption of the N-820 dye sensitizer, with a zeta-potential = – 16 mV, quite similar to the value obtained with Z-907. The iodide concentration dependence of the regeneration process rate displays in this case a large superlinear behavior. The initial slope of the $1/t_{1/2} = f([I^-])$ function establishes at $4 \cdot 10^5\ M^{-1} \cdot s^{-1}$ for $[I^-] \leq 0.1$ M but declines rapidly to reach a plateau at $[I^-] \geq 1$ M.

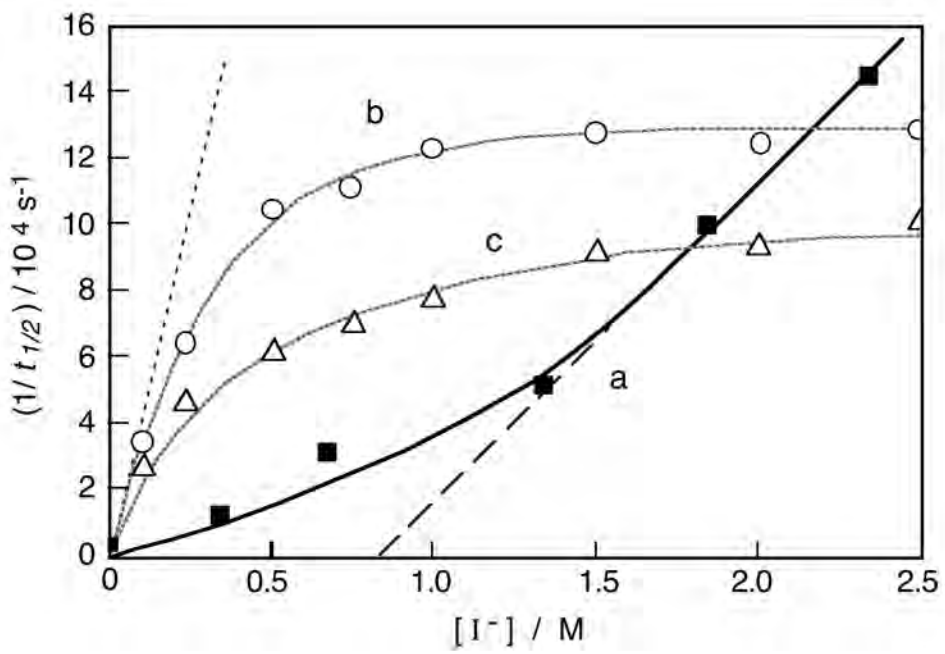

Figure 11.24 Dependence of the pseudo first-order rate constant $k_r' = 1/t_{1/2}$ of the regeneration of Z-907 (a, ■) and N-820 (b, ○) dyes adsorbed on nanocrystalline TiO_2 films upon I^- concentration in MPN. Data points c (△) were obtained with N-820-sensitized TiO_2 and 0.5 M 1-methyl-benzimidazole base (NMB) added in the electrolyte. Data set a is from ref. [110]. Data points b and c are from ref. [109].

This behavior is consistent with a Langmuir adsorption isotherm description (Eq. 11.8), where an associative interaction between I^- species and the dyed surface seems to be operative. The static reactive concentration of iodide associated with the dye layer is larger than the bulk concentration provided the mediator content is kept

relatively low. At higher I^- bulk concentrations, though, the static amount of the electrolyte able to react appears limited by a maximum surface concentration in a saturated layer. Addition in the solution of 0.5 M of 1-methyl-benzimidazole (NMB), an organic base likely to adsorb on the acidic surface of the oxide and to scavenge the protons released by the dye upon adsorption, did not affect the superlinear concentration dependence of the interception rate but reduced the maximum surface concentration by 30 % (data points c). Comparison of results obtained for both dye sensitizers then suggests that reactive iodide species are primarily kept outside of the Z-907 dye layer, involving a dynamical reaction kinetics. Surprinsingly, in the case of N-820, the regeneration process seems to proceed exclusively with a static concentration of I^- anions or (I^-, I^-) pairs adsorbed on the surface of the oxide.

Alternative redox mediator electrolytes

Despite its good performance, the triiodide/iodide couple has several drawbacks: the triiodide ion absorbs a significant part of the visible light when employed at high concentration, its aggressiveness towards silver prevents the use of this metal as current collector in large cells. More importantly, the dye regeneration is complicated by the fact that the conversion of iodide to triiodide involves the transfer of two electrons. A large driving force is therefore necessary to carry out the primary oxidation step from iodide to iodine atom or to $I_2^{-\bullet}$ species. The resulting potential mismatch between the (S^+/ S) and (I_3^-/ I^-) redox couples is responsible for a large polarization loss of nearly 0.6 V. Two electrons reduction of I_3^- at the counter electrode is hampered by a large overpotential barrier on doped tin oxide transparent electrodes that requires a catalytic coating of platinum on the counter electrode. Cheaper materials like graphite, silver or copper could however be used with a one-electron mediator of less corrosive nature.

Pseudo-halides couples $(SCN)_2$/ SCN^- and $(SeCN)_2$/ $SeCN^-$ were evaluated for their utilization in dye-sensitized solar cells. Although potentials of these mediators are

more positive than that of I_3^-/ I^-, low conversion efficiency and poor stability were obtained, which were attributed to slow interception of dye cations. Endeavors to increase the photovoltage of DSCs by replacing iodide with a one-electron, outer-sphere redox couple with a more positive oxidation potential have not fully succeeded yet, largely because of the limitations imposed by fast indirect charge recombination (dark current) and slow diffusion of the alternative mediator. It also has been inferred from intensity-modulated photovoltage spectroscopy experiments that the complex mechanism of the oxidation of iodide could in fact be essential to the energy conversion efficiency of DSCs and that attempts to use a simple one-electron redox mediator system instead are unlikely to be successful [111,112].

Organic mediators, such as quinone/ hydroquinone, phenothiazines, and triarylamine donors gave interesting results. These systems provide remarkably long-lived interfacial charge-separated pairs but show deceiving photovoltaic performances. Solid-state devices have been described, in which the liquid electrolyte present in the pores of the nanocrystalline film is replaced by a large band gap *p*-type semiconductor acting as a hole transporting medium. Parallel to this development, bis[2,6-bis(1'-butylbenzimidazol-2'-yl)pyridine]cobalt(II) complex ($Co^{II}(dbbip)_2^{2+}$) has been proposed as a redox mediator in DSC. This compound, whose oxidation potential in acetonitrile establishes at +0.36 V/ SCE (+0.6 V/ SHE, Fig. 11.21), performed best among a series of complexes $[Co^{II}(LLL)_2]^{2+}$, and is presently the only alternative mediator to rival triiodide/ iodide couple in DSCs [103,104].

Interception of N-719 dye oxidized state by electron transfer from the $Co^{II}(dbbip)_2^{2+}$ complex in dilute electrolyte was found to follow a first-order kinetics with a rate constant $k_r = 5 \cdot 10^5\ s^{-1}$. Above a threshold of 10^{-2} M, under which the cationic relay is essentially adsorbed onto the negatively charged particle surface, larger concentrations of the reduced mediator resulted in a linear increase of the apparent rate, yielding a second-order rate constant $k_r" = 2.9 \cdot 10^6\ M^{-1} \cdot s^{-1}$, approximately one order

of magnitude smaller than the values reported for iodide [13]. Contrary to the case of I^--based electrolytes, in which a cooperative effect of adsorbed cations was observed, addition of 0.1 M Li^+ did not yield any noticeable change in the interception kinetics measured with the cobalt complex dication. Static interception compensates for the intrinsically slower reduction of S^+ by $Co^{II}(dbbip)_2^{2+}$, resulting in an observed pseudo-first-order rate similar to that obtained with the triiodide/ iodide system. Partial oxidation of the mediator causes, however, a significant drop of the regeneration rate. This effect is attributed to the preferential adsorption of the tercationic species $Co^{III}(dbbip)_2^{3+}$ at the interface and canceling of the static component of the dye regeneration reaction dynamics.

Hole-transporting media

In dye-sensitized photovoltaic cells, practical advantages may be gained by the replacement of the liquid electrolyte with a solid charge-transmitting medium. Inorganic *p*-type semiconductors such as CuI and CuSCN have been proposed in this regard. Over the last two decades there has been a burst of interest, both academic and industrial, in organic semiconductors and hole transporters with the recent realization of commercial products incorporating "plastic electronics". Ideal materials must satisfy the conditions to have a work function in the 4.5 - 5.5 eV range, to undergo rapid hole exchange with the oxidized dye, implying a small reorganization energy, and to show negligible light absorption in the visible. The use of 2,2',7,7'-tetrakis (N,N-di-*p*-methoxyphenyl-amine)-9,9'-spirobifluorene (*spiro*-OMeTAD) to constitute an amorphous hole transmitting material, in conjunction with a mesoporous TiO_2 film sensitized by N-719 dye, allowed to build a solid-state dye-sensitized solar cell with high photon-to-electron conversion efficiencies [113].

Figure 11.25 shows an energetic scheme for the electron transfer processes taking place at the dye-sensitized heterojunction of such a device. Electron injection from the sensitizer's excited state into the conduction band of TiO_2 is followed by regeneration of the dye by hole injection into the hole transporting material (HTM). Conduction band electrons in the metal oxide, as well as holes in the organic medium are then transported by a hopping mechanism to the anode and the cathode, respectively. Pulsed picosecond laser photolysis showed that the hole injection from the oxidized dye-sensitizer $[Ru^{III}(dcbpy)_2(NCS)_2]^+$ into *spiro*-OMeTAD hole transporter material proceeds over a broad time ranging from < 3 ps to > 1 ns [114]. This wide time-span is attributed to a statistical distribution of the dye-hole conductor separation distances, and suggests that the dye is not perfectly and uniformly contacted by the mediator molecules. Furthermore, ns flash photolysis experiments applied to samples prepared by typical techniques used to fill the pores of the sintered TiO_2 films with the organic material have actually demonstrated that up to 30-50 % of the oxidized dye species resulting from the charge injection process are not intercepted before they recombine with conduction band electrons. Despite the large kinetic redundancy of the hole injection process compared to the back-elecron transfer, the performance of solid-state devices based on *spiro*-OMeTAD mediator is often limited by this problem.

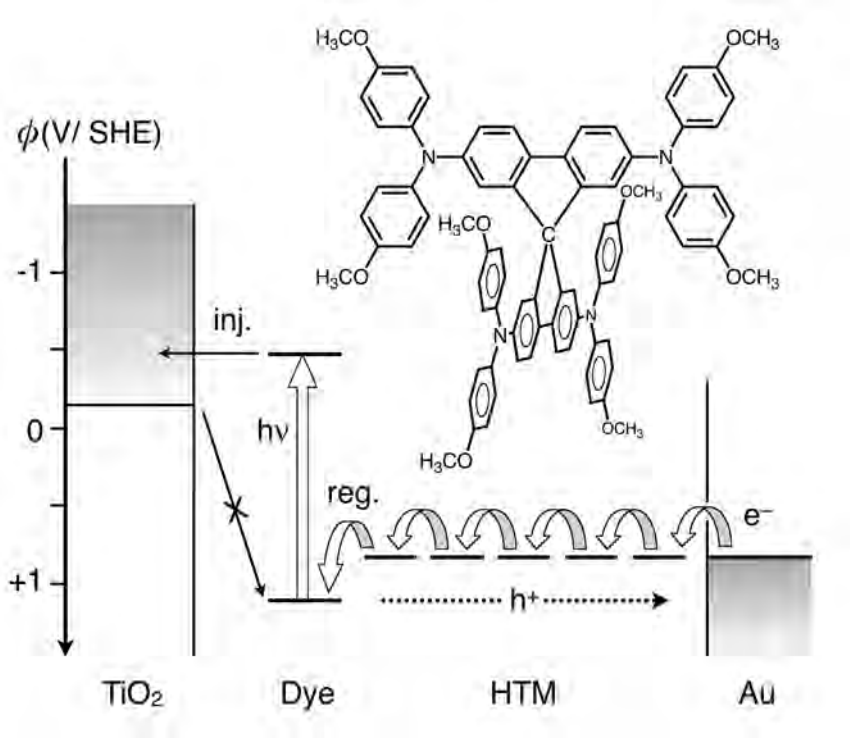

Figure 11.25 Energetic scheme of electron transfer processes taking place in a dye-sensitized TiO_2 | *spiro*-OMeTAD | Au heterojunction photovoltaic cell. Also shown is the molecular structure of the organic hole transporting material (HTM).

11.4.2 Conduction band electron - oxidized mediator recombination

Back electron transfer reaction between conduction band electrons and the oxidized form of the mediator (Eq. 11.6) is the ultimate fate of photoinjected carriers. This process manifests itself as dark current in limiting the photovoltage that can be attained in dye-sensitized photovoltaic cells. In the case of I_3^-/I^- electrolytes, one-electron reduction of triiodide leads to the now familiar $I_2^{-\cdot}$ radical species (Eq. 11.32), which yields iodide through dismutation (Eq. 11.33). A second recombination path in principle also exists, which is represented by Eq. 11.34. This process is coupled to the reduction of I_3^- (Eq. 11.32), but could also be consecutive to the production of $I_2^{-\cdot}$ by the dye cation interception reaction (Eq. 11.27).

$$I_3^- + e_{cb}^- \rightarrow I_2^{-\cdot} \quad (11.32)$$

$$2\, I_2^{-\cdot} \rightarrow I_3^- + I^- \quad (11.33)$$

$$I_2^{-\cdot} + e_{cb}^- \rightarrow 2\, I^- \quad (11.34)$$

On the surface of TiO_2 sensitized by a Ru-based dye and in the presence of iodide electrolyte, the decay of injected electrons by reaction with the oxidized mediator was followed by intensity modulated photocurrent-, microwave conductivity-, and time-resolved optical spectroscopies. This process was observed to occur within a time frame of hundreds of milliseconds to seconds. On mesoporous TiO_2 electrodes sensitized by *cis*-$Ru^{II}(dcbpy)_2(NCS)_2$, the rate of the indirect recombination reaction of injected electrons with I_3^- was reported to be second order in the electron density, with $k'' = 10^4\ M^{-1} \cdot s^{-1}$ at $[I_3^-] = 5 \cdot 10^{-2}$ M [111,112]. Such a slow reaction obviously implies the charge transfer takes place from fully thermalized and trapped carriers. It also suggests the reaction of electrons with $I_2^{-\cdot}$ (Eq. 11.34) to be unable to compete kinetically with the radical anion dismutation (Eq. 11.33), whose rate constant is $> 10^9\ M^{-1} \cdot s^{-1}$ [107].

Recombination of e_{cb}^- (TiO_2) with $Co^{III}(dbbip)_2^{3+}$ was measured directly by following the decay of the transient absorption due to the oxidized mediator species [103]. A clean pseudo-first order rate behavior was observed in this case, with a second order rate constant $k'' = 3 \cdot 10^4\ M^{-1} \cdot s^{-1}$, only slightly larger than that obtained for I_3^- electrolyte. This result demonstrates once more that the rate of the recombination is actually limited by detrapping of electrons in the solid rather than by the interfacial ET dynamics. On a general point of view, it shows that systems based on one-electron redox mediators characterized by low reorganization energy and thus able to reduce rapidly the oxidized dye species do not fatally have to pay a tribute to the indirect recombination process. Important dark current usually observed in such systems, are essentially due to the reduction of the mediator on the conducting glass that is in direct

contact with the electrolyte at the bottom of the porous titanium dioxide film. This short circuit can be decreased markedly by depositing a thin, dense TiO_2 blocking layer between the supporting electrode and the nanocrystalline film. This blocking layer is not necessary in the case of the use of iodide-based electrolytes because of the irreversibility of the I_3^-/ I^- redox couple on doped tin oxide.

As for the recombination of conduction band and trapped electrons with the oxidized dye species at the surface, the rate of the interfacial charge transfer to the oxidized mediator is expected to depend strongly on the distribution and occupancy of intra-bandgap states in the semiconductor, and therefore upon the light intensity, the applied potential bias, and the nature and concentration of adsorbates. Transport of electrons within the semiconductor nanocrystalline network to the back contact also depends upon the same phenomena. Dynamics of this process, of the transport of holes in the pores and of the electron-hole recombination at the surface are closely entangled and must then be treated globally [115].

11.4.3 Electron transport in nanocrystalline TiO_2 films

Because the macroscopic electric field across the film is negligible at normal solar light intensities due to dielectric screening by the electrolyte, transport of injected electrons to the collecting back contact is believed to occur by diffusion. This process competes with recombination. In DSCs, slow transport can thus lead to a low charge-collection efficiency and consequently to a low overall conversion efficiency.

Intensity-modulated photocurrent- (IMPS) and electrochemical impedance (EIS) spectroscopies, as well as conductivity and transient photocurrent measurements have been used to probe the transport properties of nanocrystalline TiO_2 films. The time constant obtained for the collection of injected electrons in mesoporous titania layers

lies in the millisecond domain [116,117]. Taking into account the particular morphology of the sintered film, its fractal dimension, and the percolation pathway electrons have to follow, the average transit time τ_c of photo-injected electrons to reach the back contact can be expressed by Eq. 11.32, where d is the film thickness and D_e the electron diffusion coefficient [117].

$$\tau_c = \frac{d^2}{2.35\ D_e} \tag{11.35}$$

From electron Hall mobility measurements carried out in anatase single crystals ($\mu = 18$ cm^2/ Vs) [118], a carrier diffusion coefficient at room temperature $D_e = \mu\, k_B T/ e = 0.4$ cm^2/ s is calculated. This value fed into Eq. 11.35 with $d = 12$ µm would yield a time constant for electron collection of the order of $\tau_c = 1$ µs, which is several orders of magnitude shorter than the electron lifetime measured in mesoporous systems. The slow collection has been attributed to trap-limited transport. In addition, the electron transit time is observed to decrease with increasing light intensity, a phenomenon attributed to the trap states having an exponential distribution of energies [115,117,119].

Apparent electron diffusion coefficients D_e^* and electron lifetime τ_c in mesoporous films can be extracted from IMPS and EIS spectra by applying appropriate equivalent circuits [120,121]. These parameters have been shown to predict well the photovoltaic performance of the DSC. Indeed, a majority of photogenerated carriers would be collected when the effective diffusion length L_n of electrons is larger than the film thickness d : $L_n = (D_e^* / \tau_c)^{1/2} > d$. The values of these key parameters can also be derived directly from time-resolved photocurrent measurements that do not require the application of any preconceived model or assumption [119].

Figure 11.26 shows, as an example, results of a transient photocurrent/ photovoltage study of a complete DSC based on Z-907-sensitized TiO_2 and containing

two different electrolytes. Measurements were carried out by using weak laser pulses ($\lambda = 514$ nm, $F < 100$ μJ/ cm^2, pulse duration 5 ns), superimposed on a relatively intense red light ($\lambda > 680$ nm, 120 mW/ cm^2) bias illumination provided by a cw lamp. Transient photovoltage signals were measured in open circuit conditions by connecting both electrodes of the DSC directly to an oscilloscope, whose impedance was 1 MΩ. Current transients were measured in short circuit conditions across a 20 Ω resistor load. The characteristic time constant τ could generally be fitted to one major single-exponential decay process, while the apparent diffusion coefficient D_e^* was estimated from Eq. 11.35. Electrolyte **1** contained 0.5 M free I^- (from PMII), 0.1 M I_3^- and 0.5 M NMB in MPN. Electrolyte **2** contained 0.65 M I^-, 0.05 M I_3^-, 0.5 M tBuPy and 0.1 M Li^+ in CH_3CN.

The time constants fitted from the exponential decay of the photovoltage signals (Fig. 11.26 A) were $\tau = 3.1$ ms and 7.2 ms for electrolytes **1** and **2**, respectively. In open-circuit conditions, electrons are not collected at the back electrode. Values derived for the electrons lifetime should then be comparable with the reciprocal first-order rate constant $\tau = 1/k_m$ of the indirect recombination reaction between conduction band electrons and I_3^-. Indeed, excellent agreement is found between values of k_m obtained by transient photovoltage measurements and optical experiments, in which the time course of the transient absorbance of conduction band electrons in the near-IR spectral domain is analyzed.

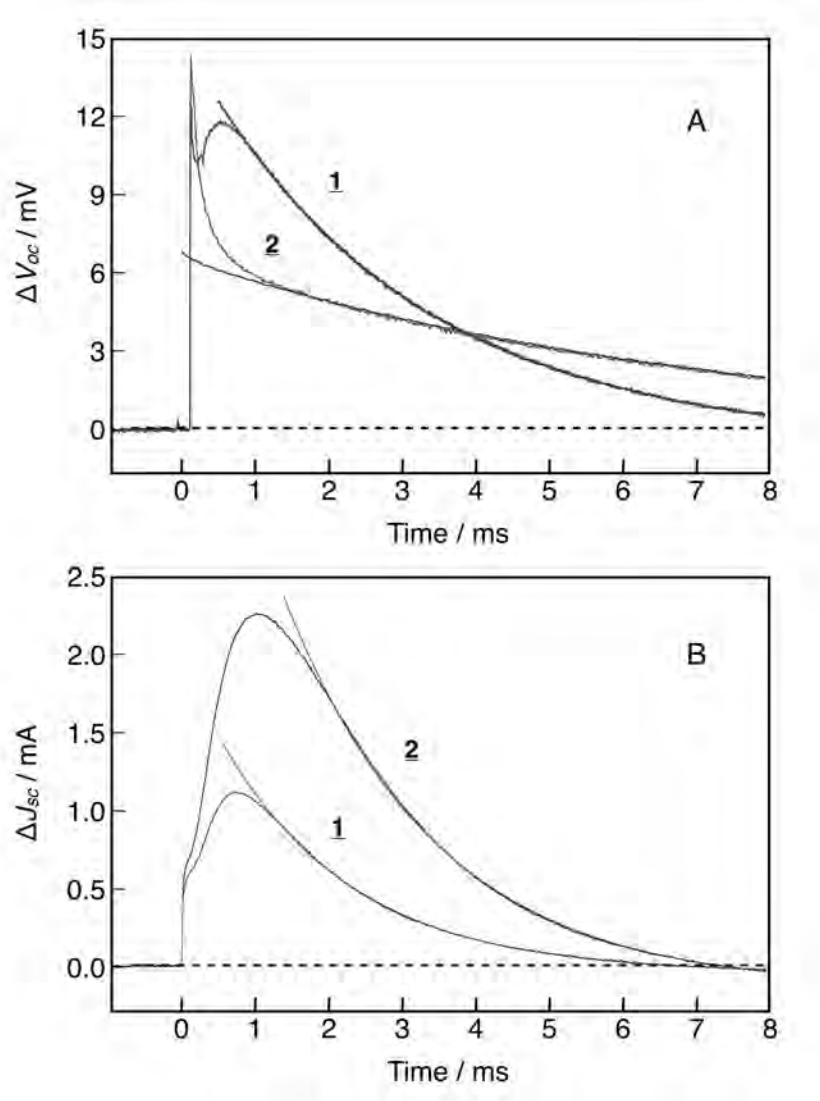

Figure 11.26 Transient photovoltage (A) and photocurrent (B) of Z-907 dye-sensitized mesoporous TiO_2 solar cells with electrolytes **1** and **2**. Lines superimposed on experimental signals are exponential fits of the decay processes. Data and conditions are that of ref. [120].

The initial peak observed on photovoltage signals is due to a large capacitive charging effect that prevents measurements during the first 1-2 ms. The same problem is observed in transient photocurrent signals (Fig. 11.26 B), where very good exponential fits could however be obtained. In this case, average electron collection time $\tau_c = 1.6$ ms and 1.9 ms were derived, yielding for a 12 μm-thick film calculated effective diffusion coefficients $D_e^* = 4 \cdot 10^{-4}$ cm^2/ s and $3 \cdot 10^{-4}$ cm^2/ s for electrolytes **1**

and **2**, respectively. In short circuit conditions, the recombination reaction is coupled to the collection of electrons at the back contact. Hence lifetimes are here shorter than those given by transient photovoltage measurements.

Comparison of the values obtained for the electron lifetimes in open- and short circuit states allows estimating the relative contribution of the recombination process. In the case of electrolyte **2**, collection of photoinjected carriers appears to take place about 4 times faster than recombination with the oxidized mediator. The recombination reaction appears to be more rapid in electrolyte **1**, which is characterized by a higher concentration of I_3^-, and an acceleration of a factor of only 2 is observed. The adverse competition of the recombination reaction in this case is also evidenced by the lower value of the photocurrent observed for the MPN-based electrolyte (ΔJ_{sc} for electrolyte **2** is 12.3 mA/ cm^2, whereas that of electrolyte **1** is only 7.9 mA/ cm^2).

In this example the high intensity of the light bias could have resulted in an electron concentration in the TiO_2 film larger than what is normally experienced under 1 sun illumination and, therefore, in an overstated recombination with the oxidized mediator. Competition of this undesired process with the ambipolar diffusion and collection of electrons and holes at electrodes should not, however, be underestimated, as it could constitute the main source of limitation of both the short-circuit current and open-circuit voltage of a dye-sensitized solar cell, in which the charge injection and dye regeneration processes have been optimized.

References

(1) Thorsmølle, V. K.; Wenger, B.; Teuscher, J.; Bauer, C.; Moser, J. E. *Chimia* **2007**, *61*, 631-634.

(2) Ardo, S.; Meyer, G. J. *Chem. Soc. Rev.* **2009**, *38*, 115-164.

(3) Moser, J.; Punchihewa, S.; Infelta, P. P.; Grätzel, M. *Langmuir* **1991**, *7*, 3012-3018.

(4) Trammel, S. A.; Meyer, T. J. *J. Phys. Chem.* **1999**, *103*, 104-107.

(5) Benkö, G.; Hilgendorff, M.; Yartsev, A. P.; Sundström, V. *J. Phys. Chem. B* **2001**, *105*, 967-974.

(6) Pelet, S.; Grätzel, M.; Moser, J. E. *J. Phys. Chem. B* **2003**, *107*, 3215-3224.

(7) Watanabe, T.; Fujishima, A.; Tatsuoki, O.; Honda, K. *Bull. Chem. Soc. Jpn.* **1976**, *49*, 355-358.

(8) Nozik, A. J. *Annu. Rev. Phys. Chem.* **1978**, *29*, 189-222.

(9) Rothenberger, G.; Fitzmaurice, D.; Grätzel, M. *J. Phys. Chem.* **1992**, *96*, 5983-5986.

(10) O'Regan, B.; Grätzel, M.; Fitzmaurice, D. *Chem. Phys. Lett.* **1991**, *183*, 89-93.

(11) Redmond, G.; Fitzmaurice, D. *J. Phys. Chem.* **1993**, *97*, 1426-1430.

(12) Lyon, L. A.; Hupp, J. T. *J. Phys. Chem. B* **1999**, *103*, 4623-4628.

(13) Pelet, S.; Moser, J. E.; Grätzel, M. *J. Phys. Chem. B* **2000**, *104*, 1791-1795.

(14) Finklea, H. O. *Semiconductor electrodes*; Elsevier: Amsterdam, 1988.

(15) Siripala, W.; Tomkievicz, M. *J. Electrochem. Soc.* **1982**, *129*, 1240-1245.

(16) Albery, W. J.; Bartlett, P. N. *J. Electrochem. Soc.* **1984**, *131*, 315-321.

(17) Hagfeldt, A.; Björkstén, U.; Grätzel, M. *J. Phys. Chem.* **1996**, *100*, 8045-8048.

(18) Schoenmakers, G. H.; Vanmaekelbergh, D.; Kelly, J. J. *J. Phys. Chem.* **1996**, *100*, 3215-3220.

(19) Monticone, S.; Tufeu, R.; Kanaev, A. V. *J. Phys. Chem. B* **1998**, *102*, 2854-2862.

(20) Sakohara, S.; Ishida, M.; Anderson, M. A. *J. Phys. Chem. B* **1998**, *102*, 10169-10175.

(21) Björkstén, U.; Moser, J.; Grätzel, M. *Chem. Mater.* **1994**, *6*, 858-863.

(22) Howe, R. F.; Grätzel, M. *J. Phys. Chem.* **1985**, *89*, 4495-4499.

(23) Howe, R. F.; Grätzel, M. *J. Phys. Chem.* **1987**, *91*, 3906-3909.

(24) Grätzel, M.; Howe, R. F. *J. Phys. Chem.* **1990**, *94*, 2566-2572.

(25) Hagfeldt, A.; Lunell, S.; Siegbahn, H. O. G. *Int. J. Quantum Chem.* **1994**, *49*, 97-104.
(26) Hagfeldt, A.; Grätzel, M. *Chem. Rev.* **1995**, *95*, 49-68.
(27) Alban, V. MSc thesis, Ecole Polytechnique Fédérale de Lausanne, 2000.
(28) Kay, A.; Humphry-Baker, R.; Grätzel, M. *J. Phys. Chem.* **1994**, *98*, 952-959.
(29) O'Regan, B.; Moser, J.; Anderson, M.; Grätzel, M. *J. Phys. Chem.* **1990**, *94*, 8720-8726.
(30) Haque, S. A.; Tachibana, Y.; Klug, D. R.; Durrant, J. R. *J. Phys. Chem. B* **1998**, *102*, 1745-1749.
(31) Haque, S. A.; Tachibana, Y.; Willis, R. L.; Moser, J. E.; Grätzel, M.; Klug, D. R.; Durrant, J. R. *J. Phys. Chem. B* **2000**, *104*, 538-547.
(32) Huber, R.; Spörlein, S.; Moser, J. E.; Grätzel, M.; Wachtveitl, J. *J. Phys. Chem. B* **2000**, *104*, 8995-9003.
(33) Nazeeruddin, M. K.; Kay, A.; Rodicio, I.; Humphry-Baker, R.; Müller, E.; Liska, P.; Vlachopoulos, N.; Grätzel, M. *J. Am. Chem. Soc.* **1993**, *115*, 6382-6390.
(34) Tachibana, Y.; Haque, S. A.; Mercer, I. P.; Moser, J. E.; Klug, D. R.; Durrant, J. R. *J. Phys. Chem. B* **2001**, *105*, 7424-7431.
(35) Nazeeruddin, M. K.; Zakeeruddin, S. M.; Humphry-Baker, R.; Jirousek, M.; Liska, P.; Vlachopoulos, N.; Shklover, V.; Fischer, C.-H.; Grätzel, M. *Inorg. Chem.* **1999**, *38*, 6298-6305.
(36) Lemon, B. I.; Hupp, J. T. *J. Phys. Chem. B* **1999**, *103*, 3797-3799.
(37) Lanzafame, J. M.; Palese, S.; Wang, D.; Miller, R. J. D.; Muenter, A. A. *J. Phys. Chem.* **1994**, *98*, 11020-11033.
(38) Miller, R. J. D.; McLendon, G. L.; Nozik, A. J.; Schmickler, W.; Willig, F. *Surface electron transfer processes*; VCH Publishers: New York, 1995.
(39) Smith, R. A. *Semiconductors*; 2nd ed.; Cambridge University Press: Cambridge, 1978.
(40) Enright, B.; Fitzmaurice, D. *J. Phys. Chem.* **1996**, *100*, 1027-1035.
(41) Asbury, J. B.; Ellingson, R. J.; Ghosh, H. N.; Ferrere, S.; Nozik, A. J.; Lian, T. *J. Phys. Chem. B* **1999**, *103*, 3110-3119.
(42) Hashimoto, K.; Hiramoto, M.; Kajiwara, T.; Sakata, T. *J. Phys. Chem.* **1988**, *92*, 4636-4640.
(43) Desilvestro, J.; Grätzel, M.; Kavan, L.; Moser, J.; Augustynski, J. *J. Am. Chem. Soc.* **1985**, *107*, 2988-2990.
(44) Moser, J.; Grätzel, M. *J. Am. Chem. Soc.* **1984**, *106*, 6557-6564.
(45) Eichberger, R.; Willig, F. *Chem. Phys.* **1990**, *141*, 159-173.

(46) Rehm, J. M.; McLendon, G. L.; Nagasawa, Y.; Yoshihara, K.; Moser, J.; Grätzel, M. *J. Phys. Chem.* **1996**, *100*, 9577-9578.

(47) Spitler, M. T.; Ehret, A.; Kietzmann, R.; Willig, F. *J. Phys. Chem. B* **1997**, *101*, 2552-2557.

(48) Koops, S. E.; O'Regan, B. C.; Barnes, P. R. F.; Durrant, J. R. *J. Am. Chem. Soc.* **2009**, *131*, 4808-4818.

(49) Hagberg, D. P.; Yum, J.; Lee, H.; De Angelis, F.; Marinado, T.; Karlsson, K. M.; Humphry-Baker, R.; Sun, L.; Hagfeldt, A.; Grätzel, M.; Nazeeruddin, M. K. *J. Am. Chem. Soc.* **2008**, *130*, 6259-6266.

(50) Xu, M.; Wenger, S.; Bala, H.; Shi, D.; Li, R.; Zhou, Y.; Zakeeruddin, S. M.; Grätzel, M.; Wang, P. *J. Phys. Chem. C* **2009**, *113*, 2966-2973.

(51) Zhang, G.; Bai, Y.; Li, R.; Shi, D.; Wenger, S.; Zakeeruddin, S. M.; Grätzel, M.; Wang, P. *Energ. Environ. Sci.* **2009**, *2*, 92-95.

(52) Moser, J. E.; Noukakis, D.; Bach, U.; Tachibana, Y.; Klug, D. R.; Durrant, J. R.; Humphry-Baker, R.; Grätzel, M. *J. Chem. Phys.* **1998**, *102*, 3649-3650.

(53) Tachibana, Y.; Moser, J. E.; Grätzel, M.; Klug, D. R.; Durrant, J. R. *J. Phys. Chem.* **1996**, *100*, 20056-20062.

(54) Das, S.; Kamat, P. V. *J. Phys. Chem. B* **1998**, *102*, 8954-8957.

(55) Durrant, J. R.; Tachibana, Y.; Mercer, I.; Moser, J. E.; Grätzel, M.; Klug, D. R. *Z. Phys. Chem.* **1999**, *212*, 93-98.

(56) Hannapel, T.; Burfeindt, B.; Storck, W.; Willig, F. *J. Phys. Chem. B* **1997**, *101*, 6799-6802.

(57) Benkö, G.; Kallioinen, J.; Korppi-Tommola, J. E. I.; Yartsev, A. P.; Sundström, V. *J. Am. Chem. Soc.* **2002**, *124*, 489-493.

(58) Asbury, J.; Anderson, N.; Hao, E.; Ai, X.; Lian, T. *J. Phys. Chem. B* **2003**, *107*, 7376-7386.

(59) Kallioinen, J.; Benkö, G.; Myllyperkiö, P.; Khriachtchev, L.; Skarman, B.; Wallenberg, R.; Tuomikoski, M.; Korppi-Tommola, J.; Sundström, V.; Yartsev, A. P. *J. Phys. Chem. B* **2004**, *108*, 6365-6373.

(60) Wenger, B.; Grätzel, M.; Moser, J. E. *J. Am. Chem. Soc.* **2005**, *127*, 12150-12151.

(61) Koops, S. E.; Durrant, J. R. *Inorg. Chim. Acta* **2008**, *361*, 663-670.

(62) Tachibana, Y.; Nazeeruddin, M. K.; Grätzel, M.; Klug, D. R.; Durrant, J. R. *Chem. Phys.* **2002**, *285*, 127-132.

(63) Kelly, C. A.; Farzad, F.; Thompson, D. W.; Meyer, G. J. *Langmuir* **1999**, *15*, 731-737.

(64) Langdon, B. T.; MacKenzie, V. J.; Asunskis, D. J.; Kelley, D. F. *J. Phys. Chem. B* **1999**, *103*, 11176-11180.

(65) Wang, P.; Wenger, B.; Humphry-Baker, R.; Moser, J. E.; Teuscher, J.; Kantlehner, W.; Mezger, J.; Stoyanov, E. V.; Zakeeruddin, S. M.; Grätzel, M. *J. Am. Chem. Soc.* **2005**, *127*, 6850-6856.

(66) Moser, J. E.; Wolf, M.; Lenzmann, F.; Grätzel, M. *Z. Phys. Chem.* **1999**, *212*, 85-92.

(67) Liu, F.; Meyer, G. J. *Inorg. Chem.* **2003**, *42*, 7351-7353.

(68) Burfeindt, B.; Hannappel, T.; Storck, W.; Willig, F. *J. Phys. Chem.* **1996**, *100*, 16463-16465.

(69) Asbury, J. B.; Wang, Y. Q.; Lian, T. *J. Phys. Chem. B* **1999**, *103*, 6643-6647.

(70) Grätzel, M.; Moser, J. E. In *Electron Transfer in Chemistry*; Balzani, V., Gould, I. R., Eds.; Wiley-VCH: Weinheim, 2001; Vol. 5, p 589-644.

(71) Bauer, C.; Pelet, S.; Wenger, B.; Grätzel, M.; Moser, J. E. **2003**, unpublished results.

(72) Asbury, J. B.; Hao, E. C.; Wang, Y. Q.; Lian, T. Q. *J. Phys. Chem. B* **2000**, *104*, 11957-11964.

(73) Wenger, B.; Bauer, C.; Nazeeruddin, M. K.; Comte, P.; Zakeeruddin, S. M.; Grätzel, M.; Moser, J. E. *Proc. SPIE* **2006**, *6325*, 63250V.

(74) Bauer, C.; Teuscher, J.; Pelet, S.; Wenger, B.; Bonhôte, P.; Nazeeruddin, M. K.; Zakeeruddin, S. M.; Comte, P.; Grätzel, M.; Moser, J. E. *J. Phys. Chem. C* **2010**, *114*, 0000.

(75) Piotrowiak, P.; Galoppini, E.; Wei, Q.; Meyer, G. J.; Wiewior, R. *J. Am. Chem. Soc.* **2003**, *125*, 5278-5279.

(76) Ernstorfer, R.; Felber, S.; Storck, W.; Galoppini, E.; Wei, Q.; Willig, F. *Res. Chem. Intermed.* **2005**, *31*, 643-647.

(77) Moser, J. E.; Grätzel, M. *Chem. Phys.* **1993**, *176*, 493-500.

(78) Duncan, W. R.; Prezhdo, O. V. *J. Phys. Chem. B* **2005**, *109*, 365-373.

(79) Nawrocka, A.; Krawczyk, S. *J. Phys. Chem. C* **2008**, *112*, 10233-10241.

(80) Huber, R.; Moser, J. E.; Grätzel, M.; Wachtveitl, J. *J. Phys. Chem. B* **2002**, *106*, 6494-6499.

(81) Moser, J. E. *Nat. Mater.* **2005**, *4*, 723-724.

(82) Bonhôte, P.; Moser, J. E.; Humphry-Baker, R.; Vlachopoulos, N.; Zakeeruddin, S. M.; Walder, L.; Grätzel, M. *J. Am. Chem. Soc.* **1999**, *121*, 1324-1336.

(83) Bonhôte, P.; Gogniat, E.; Tingry, S.; Barbé, C.; Vlachopoulos, N.; Lenzmann, F.; Comte, P.; Grätzel, M. *J. Phys. Chem. B* **1998**, *102*, 1498-1507.

(84) Dang, X. J.; Hupp, J. T. *J. Am. Chem. Soc.* **1999**, *121*, 8399-8400.

(85) Kuciaukas, D.; Freund, M. S.; Gray, H. B.; Winkler, J. R.; Lewis, N. S. *J. Phys. Chem. B* **2001**, *105*, 392-403.

(86) Clifford, J. N.; Palomares, E.; Nazeeruddin, M. K.; Grätzel, M.; Nelson, J.; Li, X.; Long, N. J.; Durrant, J. R. *J. Am. Chem. Soc.* **2004**, *126*, 5225-5233.

(87) Weng, Y. X.; Wang, Y. Q.; Asbury, J. B.; Ghosh, H. N.; Lian, T. *J. Phys. Chem. B* **2000**, *104*, 93-104.

(88) Nelson, J.; Haque, S. A.; Klug, D. R.; Durrant, J. R. *Phys. Rev. B* **2001**, *63*, 205321.

(89) Nelson, J.; Chandler, R. E. *Coord. Chem. Rev.* **2004**, *248*, 1181-1194.

(90) Kelly, C. A.; Farzad, F.; Thompson, D. W.; Stipkala, J. M.; Meyer, G. J. *Langmuir* **1999**, *15*, 7047-7054.

(91) Rothenberger, G.; Moser, J.; Grätzel, M.; Serpone, N.; Sharma, D. K. *J. Am. Chem. Soc.* **1985**, *107*, 8054-8059.

(92) Haque, S. A.; Handa, S.; Peter, K.; Palomares, E.; Thelakkat, M.; Durrant, J. R. *Angew. Chem. Int. Ed.* **2005**, *44*, 5740-5744.

(93) Bell, T. D. M.; Pagba, C.; Myahkostupov, M.; Hofkens, J.; Piotrowiak, P. *J. Phys. Chem. B* **2006**, *110*, 25314-25321.

(94) Clifford, J. N.; Yahioglu, G.; Milgrom, L. R.; Durrant, J. R. *Chem. Commun.* **2002**, 1260-1261.

(95) Hilgendorff, M.; Sundström, V. *J. Phys. Chem. B* **1998**, *102*, 10505-10514.

(96) Liu, D.; Fessenden, R. W.; Hug, G. L.; Kamat, P. V. *J. Phys. Chem. B* **1997**, *101*, 2583-2590.

(97) Ghosh, H. N.; Asbury, J. B.; Weng, Y. X.; Lian, T. Q. *J. Phys. Chem. B* **1998**, *102*, 10208-10215.

(98) Nelson, J. *Phys. Rev. B* **1999**, *59*, 15374-15380.

(99) Datta, J.; Bhattacharya, A.; Kundu, K. K. *Bull. Chem. Soc. Jpn.* **1988**, *61*, 1735-1742.

(100) Nasr, C.; Hotchandani, S.; Kamat, P. V. *J. Phys. Chem. B* **1998**, *102*, 4944-4951.

(101) Alebbi, M.; Bignozzi, C. A.; Heimer, T. A.; Hasselmann, G. M.; Meyer, G. J. *J. Phys. Chem. B* **1998**, *102*, 7577-7581.

(102) Wang, X.; Stanbury, D. M. *Inorg. Chem.* **2006**, *45*, 3415-3423.

(103) Nusbaumer, H.; Moser, J. E.; Zakeeruddin, S. M.; Nazeeruddin, M. K.; Grätzel, M. *J. Phys. Chem. B* **2001**, *105*, 10461-10464.

(104) Nusbaumer, H.; Zakeeruddin, S. M.; Moser, J. E.; Grätzel, M. *Chem. Eur. J.* **2003**, *9*, 3756-3763.

(105) Clifford, J. N.; Palomares, E.; Nazeeruddin, M. K.; Grätzel, M.; Durrant, J. R. *J. Phys. Chem. C* **2007**, *111*, 6561-6567.

(106) Privalov, T.; Boschloo, G.; Hagfeldt, A.; Svensson, P. H.; Kloo, L. *J. Phys. Chem. C* **2009**, *113*, 783-790.

(107) Fitzmaurice, D.; Frei, H. *Langmuir* **1991**, *7*, 1129-1137.

(108) Wang, P.; Zakeeruddin, S. M.; Moser, J. E.; Nazeeruddin, M. K.; Sekiguchi, T.; Grätzel, M. *Nat. Mater.* **2003**, *2*, 498-498.

(109) Andres, J.; Teuscher, J.; Zakeeruddin, S. M.; Nazeeruddin, M. K.; Moser, J. E. **2007**, unpublished results.

(110) Zhang, Z.; Ito, S.; Moser, J. E.; Zakeeruddin, S. M.; Grätzel, M. *ChemPhysChem* **2009**, *11*, 8886-8894.

(111) Fisher, A. C.; Peter, L. M.; Ponomarev, E. A.; Walker, A. B.; Wijayantha, K. G. U. *J. Phys. Chem. B* **2000**, *104*, 949-958.

(112) Duffy, N. W.; Peter, L. M.; Rajapakse, R. M.; Wijayantha, K. G. U. *J. Phys. Chem. B* **2000**, *104*, 8916-8919.

(113) Bach, U.; Lupo, D.; Comte, P.; Moser, J. E.; Weissortel, F.; Salbeck, J.; Spreitzer, H.; Grätzel, M. *Nature* **1998**, *395*, 583-585.

(114) Bach, U.; Tachibana, Y.; Moser, J. E.; Haque, S. A.; Durrant, J. R.; Grätzel, M.; Klug, D. R. *J. Am. Chem. Soc.* **1999**, *121*, 7445-7446.

(115) Peter, L. *J. Electroanal. Chem.* **2007**, *599*, 233-240.

(116) Kopidakis, N.; Schiff, E. A.; Park, N. G.; van de Langemaat, J.; Frank, A. J. *J. Phys. Chem. B* **2000**, *104*, 3930-3936.

(117) van de Langemaat, J.; Frank, A. J. *J. Phys. Chem. B* **2001**, *105*, 11194-11205.

(118) Forro, L.; Chauvet, O.; Emin, A.; Zuppiroli, L.; Berger, H.; Lévy, F. *J. Appl. Phys.* **1994**, *75*, 633-635.

(119) Benkstein, K. D.; Kopidakis, N.; van de Langemaat, J.; Frank, A. J. *J. Phys. Chem. B* **2003**, *107*, 7759-7767.

(120) Wang, Q.; Moser, J. E.; Grätzel, M. *J. Phys. Chem. B* **2005**, *109*, 14945-14953.

(121) Bisquert, J.; Vikhrenko, V. S. *J. Phys. Chem. B* **2004**, *108*, 2313-2322.